THE ASTROPHYSICAL JOURNAL SUPPLEMENT SERIES, 125:99–121, 1999 November
© 1999. The American Astronomical Society. All rights reserved. Printed in U.S.A.

PRECISION VELOCITY FIELDS IN SPIRAL GALAXIES. I. NONCIRCULAR MOTIONS AND RMS NOISE IN DISKS

CHARLES BEAUVAIS AND G. BOTHUN
Department of Physics, University of Oregon, Eugene, OR 97403; torch@jps.net, nuts@bigmoo.uoregon.edu
Received 1998 October 21; accepted 1999 June 3

ABSTRACT

Investigation of the symmetry of the major- and minor-axis rotation curves reveals strong evidence of nonconcentric gas orbits with the maximum center shift of $\sim$300 pc. Comparisons between kinematic and photometric structure (e.g., position angles, inclinations, centers) show considerable noise on small scales. Although large-scale averages are in agreement, this noise is a matter of some concern in the application of the Tully-Fisher method to disk galaxies. Moreover, cases of significant misalignment in position angle between the inner and outer disks are seen in two of the sample galaxies and may indicate the transition between luminous and dark-matter–dominated regions (i.e., where the maximum-disk hypothesis begins to fail).

The kinematic disk models are used to find the residual velocity fields, and typical residuals are found to be 10–15 km s^{-1} over regions 0.5–1.5 kpc in diameter. Correlations are shown to exist between the residual velocity fields and both the Hα intensity and the velocity dispersion images. This suggests that kinematic feedback to the gas from star formation is an important source of noncircular motion. However, the relative quiescence of the large-scale velocity field indicates that the effect does not cause a significant deviation from circular symmetry, kinematically indicating that star formation is not a hidden parameter in the Tully-Fisher relation. Finally, the residual velocity fields are examined for signs of noncircular orbits by looking for azimuthal angular harmonics that would be present if disk galaxies are embedded in a triaxial dark matter potential. For our sample we find the ellipticity of the gas orbits to be $\lesssim$0.08, which implies the potential is relatively round. This is consistent with disks being maximal.

Subject headings: galaxies: kinematics and dynamics — techniques: interferometric

1. INTRODUCTION

The study of velocity fields in spiral galaxies have been traditionally done using 21 cm H I emission as the tracer feature. This allows the kinematics and dynamics of the gas to be explored on large scales, typically at a resolution of a few kiloparsecs. Early efforts by Rots (1975), van der Hulst (1979), Bosma (1981), and Gottesman (1982) showed the power of these techniques in improving our physical understanding of disk galaxies and their implied mass distributions. The large-scale dynamics, as manifested by the observed motion of the gas, also forms the basis for the assertion that disk galaxies contain substantial amounts of nonluminous material (e.g., Kent 1986). In addition to probing the mass distribution, the large-scale behavior of the gas is a highly useful diagnostic to compare the observed radial and tangential streaming motions against predictions of density wave theory (e.g., Yuan & Cheng 1989) and to determine critical components such as the inner and outer Lindblad resonances as well as the corotation radius (see Adler & Westphal 1996; Canzian & Allen 1997). On the other hand, the large-scale gaseous component in some disk galaxies can show kinematic features that suggest the complete absence of density waves (Thornley & Mundy 1997).

Since the beam size associated with 21 cm interferometric observations is usually at least as large as the disk scale length of the target galaxy, very little small-scale structure in the velocity field can be detected in this manner. Improved spatial resolution can be achieved when using CO as the tracer gas (e.g., Turner & Hurt 1992), but such gas is usually strongly confined to the spiral arms and/or nuclear regions and is not, therefore, a pervasive tracer of disk galaxy kinematics. To achieve significantly better spatial resolution requires a tracer gas that radiates at optical wavelengths and instrumentation that allows this tracer gas to be mapped in a two-dimensional fashion analogous to 21 cm interferometry.

The best candidate for this is, of course, Hα emission associated with the general star formation rate in a galactic disk. The two-dimensional kinematics of this gas can be effectively mapped by using a Fabry-Perot (FP) detector which can provide information on the kinematics of disk galaxies on a spatial scale of a few arcseconds. Moreover, since many late-type spirals have ubiquitous star formation, Hα-emitting gas is a pervasive component of the optical disk. FP observations at Hα of external galaxies were first performed photographically by Tully (1972) in his detailed study of the kinematics and dynamics of M51 (see Tully 1974). Following the pioneering work of Tully, Deharveng & Pellet (1975) performed a kinematical and dynamical study of M31 using Hα as the tracer gas, and Dubout et al. (1976) made the first observations of M33. The first systematic studies of the velocity fields of late-type spirals using an FP detector are those of de Vaucouleurs & Pence (1980) and Davoust & de Vaucouleurs (1980). Marcelin et al. (1982) extended this technique to the more complex velocity

fields that arise in interacting galaxies through their observations of NGC 5128. Williams, Caldwell, & Schommer (1984) first used a CCD as the detector being the Fabry-Perot in their study of the ionized hydrogen in M82.

To date, FP observations of spiral galaxies at Hα have been used to construct high signal-to-noise ratio (S/N) rotation curves for several late-type galaxies (e.g., Marcelin, Boulesteix, & Georgelin 1985; Bonnarel et al. 1988; Pence, Taylor, & Atherton 1990; Corradi et al. 1991; Cecil, Wilson, & Tully 1992; Vogel et al. 1993; Veilleux, Cecil, & Bland-Hawthorn 1995; Sicotte, Caignan, & Durand 1996; Ryder et al. 1998; Jimenez-Vicente et al. 1999). Most of those studies have concentrated only on specific galaxies and not samples. By far the largest single sample comes from Schommer et al. (1993, hereafter SBWM), who observed approximately 100 galaxies in the Hydra-Centaurus regions. In addition to late-type spirals, FP observations have been used to study the detailed velocity field in barred spirals (e.g., Teuben et al. 1986; Pence et al. 1988; Schommer et al. 1988; Duval et al. 1991; Regan et al. 1996). Finally, strongly interacting galaxies are natural FP targets, so that detailed comparisons can be done between observations and models of interacting galaxies (see Marcelin et al. 1987; Unger et al. 1990; Caulet et al. 1992; Mihos & Bothun 1997, 1998).

The resolution and overall data qualities of the previously cited observations show considerable variation. It is the aim of the present study to improve upon this foundation by performing FP observations with higher S/N and velocity resolution than have been achieved before. Our goal is to derive as precise a velocity field as possible. As emphasized by Lyakhovich et al. (1997), recovery of the full vector velocity field can result in a fairly precise determination of the mass distribution within that disk. Potentially, this means that the small-scale mass distribution can be compared with the light distribution to provide a more effective constraint on the maximal disk hypothesis, currently a contentious issue (see Sackett et al. 1994; Sackett 1997; McGaugh & de Blok 1998; Courteau & Rix 1999). Since the S/N of FP observations is limited only by Hα surface brightness per pixel, in general there is no strong radial degradation in the quality of the velocity field. That is, the errors on the velocity measurements at less than 1 scale length are similar to those present at 3 scale lengths. The major limiting factor is the filling factor of Hα emission within the disk and the velocity resolution of the observations.

In this paper, we present the results of FP Hα observations of seven spiral galaxies that have large disk volume filling factors of Hα emission and velocities less than 4000 km s^{-1}. For these galaxies we are able to determine precision velocity fields (errors ≤ 15 km s^{-1}) over most of the optical extent of the disk on a subkiloparsec scale. We use these data to study noncircular motions in spiral galaxies. The presence of noncircular motions in spiral galaxies can have a considerable impact on the shape of the rotation curve and thus on the shape and amount of dark matter inferred. In turn, this impacts one of the major assumptions in the Tully-Fisher (TF) relation, namely, that disk galaxies are circularly symmetric in both a photometric and a kinematic sense. To first order, the modes scatter observed in the TF relation does imply that, on large scales, the velocity field must be fairly quiet (see Tully & Fouqué 1985). We are interested here in detecting possible systematic departures from circular symmetry, as such departures could easily be an important source of scatter in the TF relation (Franx & de Zeeuw 1992; Bothun & McGaugh 1999). Currently, there are very few available data that constrain the actual small-scale rms noise in the velocity field, and the sample discussed here will help to overcome this limitation.

There are many possible sources for the occurrence of noncircular motions. The presence of a bar will cause local deviations due to the elongated potential (e.g., Amram et al. 1992, 1996). Strong spiral structure can introduce shocks and streaming motions in the gas (Marcelin et al. 1985). Radiation pressure from young stars can drive gas motions, and this kinematic feedback to the ISM can be directly explored in these data, as the Hα strength is directly related to the star formation rate. In addition, any perturbation in the local mass density within the disk will produce a corresponding perturbation in the orbits, so, in effect, the construction of precision velocity fields can reveal a lumpy mass distribution if it exists. Finally, warping in the inner disk would lead to noncoplanar gas orbits that would effectively render the derived rotation curve meaningless.

The possibility of exploring all of the above-mentioned effects via a single data set has motivated our FP study of seven galaxies whose angular diameters roughly match the field of view of the instrument. This paper reports the initial results of that study. The bulk of this paper is related to describing the data reduction and the use of the tilted ring model to extract the velocity field from the FP data cube. This is fully discussed in § 2. In § 3 we present the derived velocity fields and discuss evidence for noncircular motions in these disks. We also show how the velocity fields can be reconstructed from modeling and how such models lead to firm constraints on the rms noise present in the overall disk velocity field. Concluding remarks are presented in § 4. Future papers in this series will explore other aspects of this rich data set, including the extraction of rotation curves and a comparison between dynamical features and the local star formation rate in the disk.

2. OBSERVATIONS AND DATA REDUCTION

Imaging Fabry-Perot data were taken for a number of nearby late-type disk galaxies explicitly selected to have an angular size well matched to the effective field of view of the instrument ($\sim 5'$). While we observed more galaxies that are discussed here, our final sample of seven galaxies was selected on the basis of the overall quality of the data and is listed in Table 1. The sample is certainly not complete but hopefully is representative of late-type disk galaxies that span a large range of disk mass. In Table 1, column (1) gives the galaxy identification, column (2) gives the major and minor axes, column (3) is B_T, column (4) is the heliocentric radial velocity, column (5) is the observed $B-R$ color (i.e., not corrected for foreground or internal reddening), while column (6) gives the derived maximum circular velocity (from Beauvais 1997). Finally, column (7) gives the linear resolution of the data, in units of parsecs per arcsecond. Distances to individual galaxies were obtained from either SBWM or Bureau, Mould, & Staveley-Smith (1996). As the seeing was approximately $1''.5$ in the combined FP cube, the last column shows that we are effectively sampling the velocity field on the subkiloparsec scale.

The data were acquired with the 1.5 m telescope located at CTIO on the nights of 1994 November 14–19. We used the Rutgers Imaging Fabry-Perot in the wide-band mode

TABLE 1

THE SAMPLE

Galaxy Name (1)	$a \times b$ (arcmin) (2)	B_T (mag) (3)	V_{sys} (km s^{-1}) (4)	$B-R$ (mag) (5)	V_{max} (km s^{-1}) (6)	Scale (arcsec pc^{-1}) (7)
ESO 358–G63.....	4.7 × 1.3	12.60	1932	1.10	130	75
ESO 437–G30.....	3.1 × 0.6	13.65	3759	1.50	200	210
NGC 1292.....	3.0 × 1.3	12.80	1367	1.00	105	75
NGC 1406.....	3.8 × 0.8	12.40	1075	1.20	165	75
NGC 2417.....	2.8 × 1.9	12.80	3184	1.20	190	140
NGC 3463.....	1.5 × 0.7	13.75	3950	1.40	215	205
IC 2559	1.7 × 0.7	14.35	2974	1.35	140	130

(FWHM = 2 Å), ordering filters from the standard CTIO set, and their TEK1 1k CCD. The combination of telescope and CCD gave a resolution of 0.″65 pixel^{-1}. Between 15 and 30 frames were taken for each galaxy, depending on the individual mass and inclination, to obtain full line-width coverage. Each frame was a 300 s exposure and was visually inspected in real time to determine when the end of the Hα flux was reached in velocity space.

Calibration frames were taken at regular intervals to correct for drift in both the zero point and the position of the optical axis. Flat-field and bias images were taken at each wavelength for processing. The individual frames were debiased, trimmed, and flat-fielded in the usual way with standard IRAF tasks, corrected for air mass [assuming an extinction of 0.09 mag (air mass)$^{-1}$], aligned to a common center, and then assembled into data cubes. The reduction of the data to cubes follows the procedure outlined in detail by SBWM. For each pixel in a data cube, the z-column represents the line profile of the gas imaged by that pixel (once proper corrections are made for the position of the optical axis in each frame). The line profiles (flux as a function of wavelength or velocity) of each pixel were fitted to recover four parameters: the continuum level (background), the position of the peak (line-of-sight [LOS] velocity, v_{LOS}), the velocity dispersion (half-width), and the peak Hα intensity (above background). The parameters and their errors were put into image maps for subsequent analysis.

2.1. *The Fit Algorithm*

While a number of procedures exist for fitting the line profiles of a Fabry-Perot data cube, it remains somewhat unclear what kind of profile shape should be used. The procedure of SBWM fitted Gaussian line profiles using a least squares minimization procedure to identify the best fit. The analysis employed here uses a more rigorous procedure. To begin with, a χ^2 minimization routine was substituted for the least squares minimization routine. The new routine was more stable, and the parameters were less sensitive to the initial estimates. A good initial estimate of the parameters was important for either fit algorithm to converge, especially in areas of poor S/N, so a new method for computing the estimates was devised. To remove spurious fits, a series of cuts was introduced. A minimum flux level was required, and pixels whose intensity fell below this were discarded and a failure code output to the image maps. This was adjusted for each galaxy, along with the smoothing length (see below), to maximize the area of the galaxy with reliable fits.

The only major modification to the raw data involved data smoothing. In regions of low S/N it is desirable to average the flux over some region in each frame of the cube. The line profiles obtained from the smoothed data are more regular and have smaller errors, increasing the chance of a successful fit to the profile. SBWM smooth on a 3 × 3 pixel scale for pixels with low S/N, but use no smoothing otherwise. Another standard code for fitting line profiles obtained from B. Weiner (1996, private communication) uses several different smoothing lengths, depending on the value of S/N. Such a variable smoothing length allows the best spatial resolution possible at each pixel while still guaranteeing that a fit is found if possible, but it also introduces artificial correlations between the various parameters.

To avoid these correlations, a constant smoothing length was used for all pixels in each data cube. The smoothing length was chosen to give the best spatial resolution for each galaxy, while giving good coverage by successfully fitting a large fraction of the low S/N pixels. For the galaxies in the sample, the seeing (1″) was larger than the individual pixel scale, which resulted in overlap between adjacent pixels. The alignment process used in the assembly of the data cubes also introduces a slight uncertainty in the position of individual pixels in the data cube. For these reasons, a minimum smoothing size of 3 × 3 pixels was chosen. This is slightly larger than the averaging seeing in the final image map. Smoothing every pixel allowed the use of rms deviations rather than Poisson counting statistics for the error estimates on the line profile. These were typically smaller than the Poisson errors, although they exhibited the same sort of dependence on the flux level, i.e., greatest in the profile peaks and smaller along the sides of the peaks. The smaller errors resulted in a better determination of the parameters. It also effectively removed points contaminated by cosmic-ray events from the fits by assigning them enormous errors, obviating the need for a separate screening procedure.

2.2. *Optimizing the Line Profiles*

The primary consideration in the reduction of Fabry-Perot data lies in the choice of fitting function used to model the line profile. Of interest here is the most robust and accurate way of determining the total flux under the line and its width. Issues of determining the line center are generally immune to the choice of fitting function. In the past, Gaussians have been the function of choice, since they are easily calculated and provide a reasonable approximation to the data. However, the Gaussian tends to under-

represent the data in regions of high intensity. This can compromise the accuracy of the integrated flux under the line (i.e., the intensity). Recently, Voigt functions have been gaining in popularity (e.g., Mihos & Bothun 1997, 1998). As the convolution of a Gaussian with a Lorentzian, the Voigt function has two dispersion components allowing the width to be adjusted separately (but not independently) in the peak and the tails.

To compare the performance of the two functions, a large number of profiles (300+) were modeled, and for completeness a Lorentzian was tried as well. Sample line profile fits are shown in Figure 1. Listed for each of the fits are the χ^2, Q (the χ^2 probability function, indicating the goodness of fit), and the LOS velocity. The χ^2 values (and thus Q) were found to be dominated by the continuum data points in the line profile whose errors are small. Thus, even fits with large

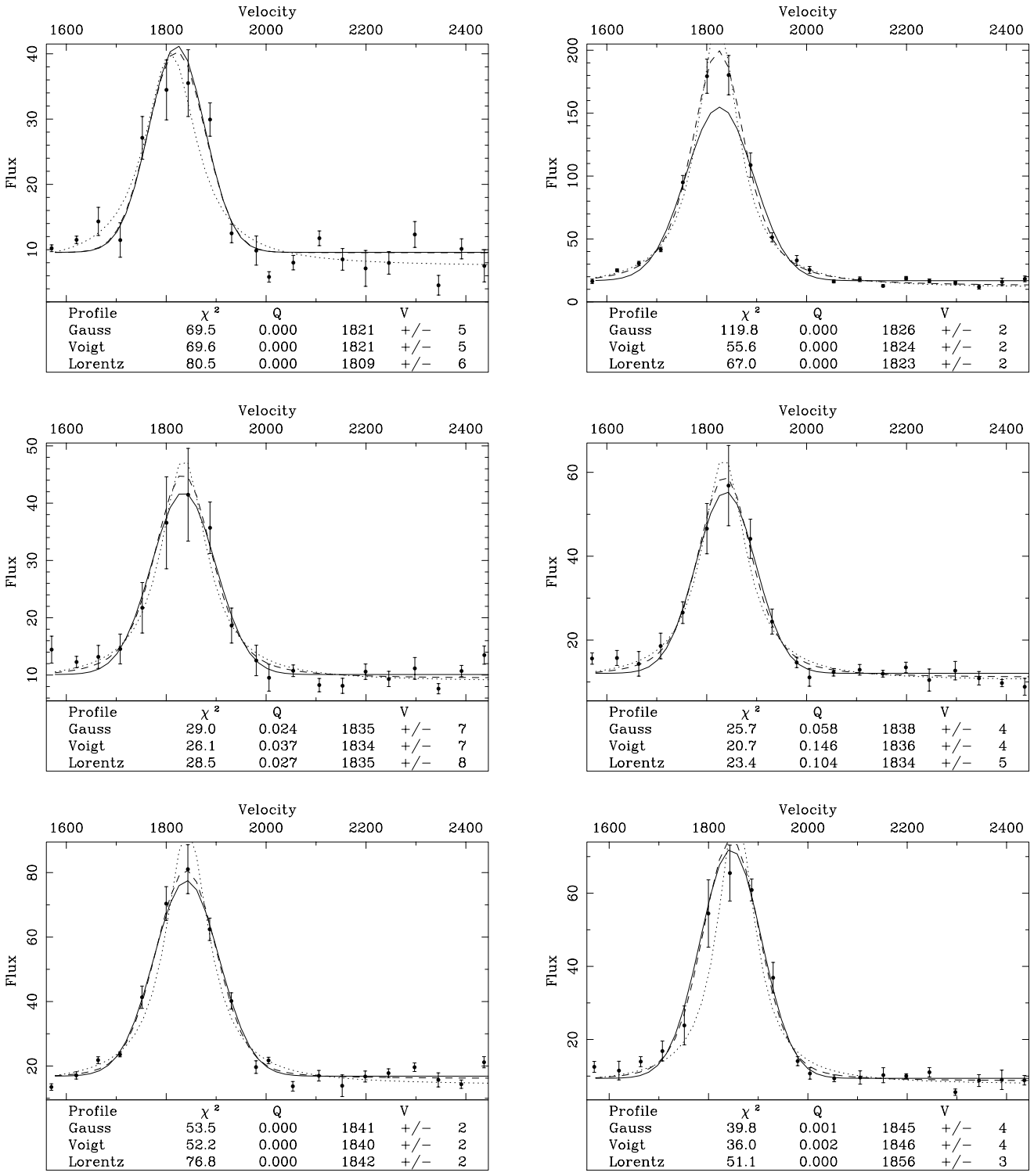

FIG. 1.—Sample line profiles fitted with Gaussian (*solid line*), Lorentzian (*dotted line*), and Voigt (*dashed line*) functions. The value of χ^2, Q (goodness of fit), and central (peak) velocity are indicated for each model.

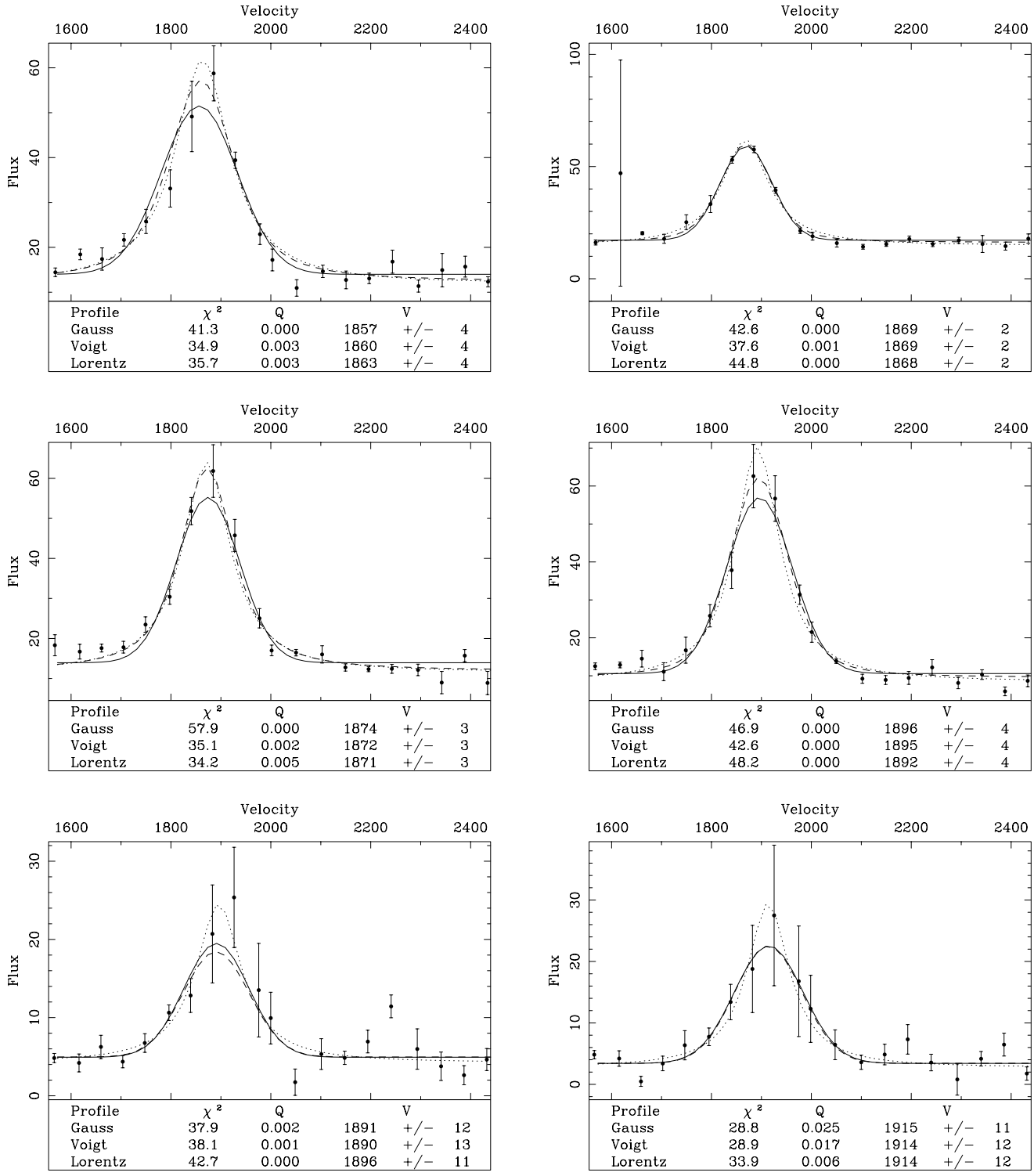

FIG. 1.—*Continued*

χ^2 (and small Q) provide a good fit to the data. That said, the Voigt profile gave the best fit. As noted earlier, the Gaussian tended to be overly short both in the peak and at its base. The Lorentzian was often too tall and too narrow, allowing systematic shifts in $V_{\rm LOS}$ caused by the asymmetry in the size of the error bars across the peak. Although the Voigt function gave the best fit to the data, the Gaussian gave an identical estimate of $V_{\rm LOS}$ in every case. Where the Voigt function surpassed the Gaussian was in providing a better estimate of the intensity and the integrated flux (area under the line profile), thus providing more reliable Hα photometry.

The added degree of freedom makes the Voigt function a better fit to the data, but it also has a major drawback. The interdependence of the dispersion components made it impossible to unambiguously determine the two individually. This resulted in large errors on the dispersion, typically greater than 35% and often much higher, and the errors on the intensity ran higher than 30% but often went as high as 150%. Another difficulty with the Voigt function

was that for the majority of the profiles the fit failed to converge at all unless run interactively. One remedy for this, employed by the standard codes that use Voigt functions to model the line profiles, is to use a four-parameter Voigt function, holding the Lorentzian component of the dispersion fixed. Sample line profiles fitted in this manner are shown in Figure 2. This greatly increased the number of profiles successfully fitted, but it also removed most of the advantage gained by using the Voigt function. Since the Gaussian is a good model for low-intensity profiles, the Lorentzian component of the dispersion must be kept small, making the two nearly identical for high-intensity profiles. Thus, the four-parameter Voigt function does not give any better photometry than the simple Gaussian.

As a final check on the utility of the various functions, the entire velocity field of E358 was fitted with Gaussian, Lor-

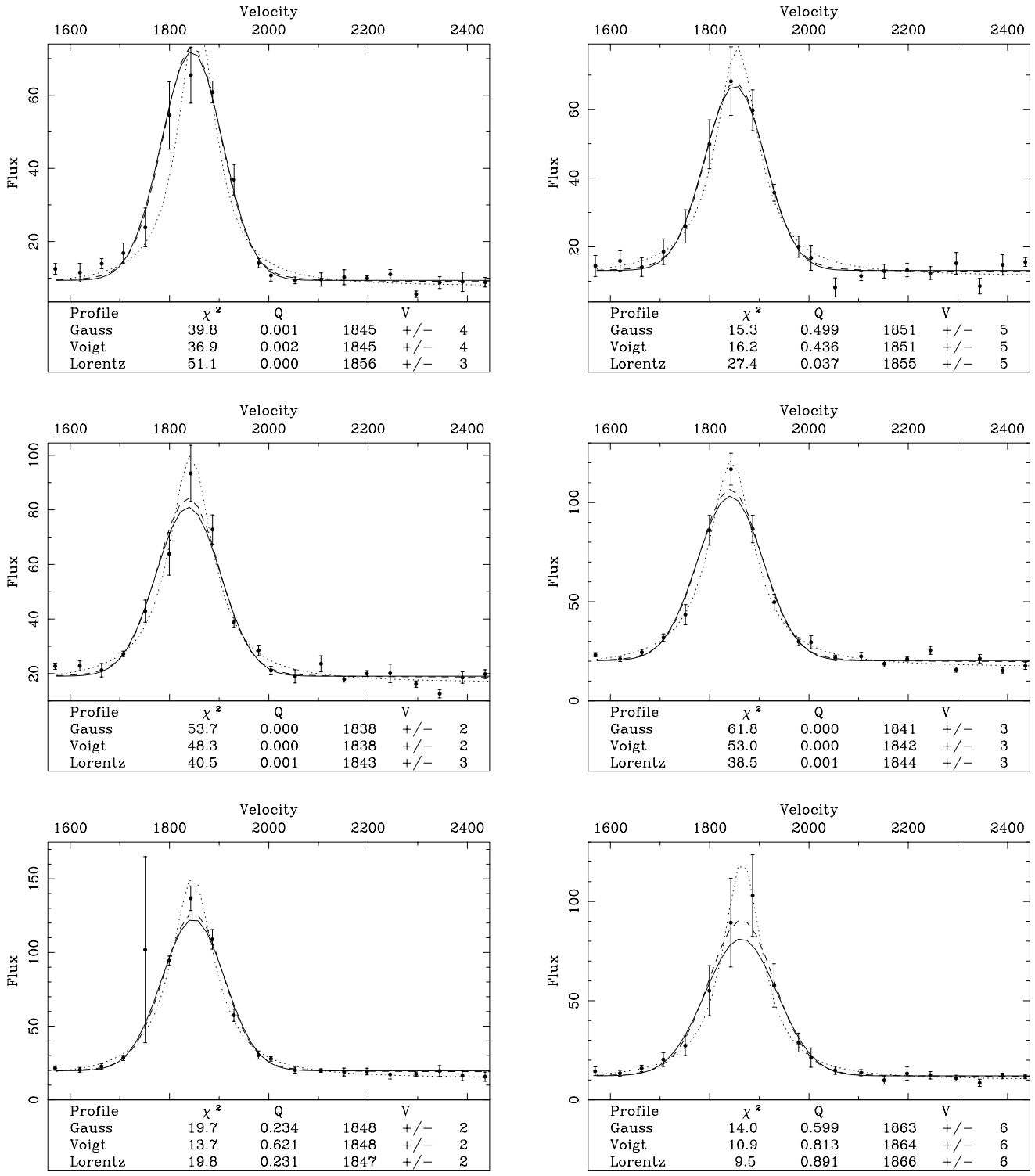

FIG. 2.—Sample line profiles fitted holding the Lorentzian component of the dispersion fixed—Gaussian (*solid line*), Lorentzian (*dotted line*), and four-parameter Voigt (*dashed line*) functions. The value of χ^2, Q (goodness of fit), and central (peak) velocity are indicated for each model.

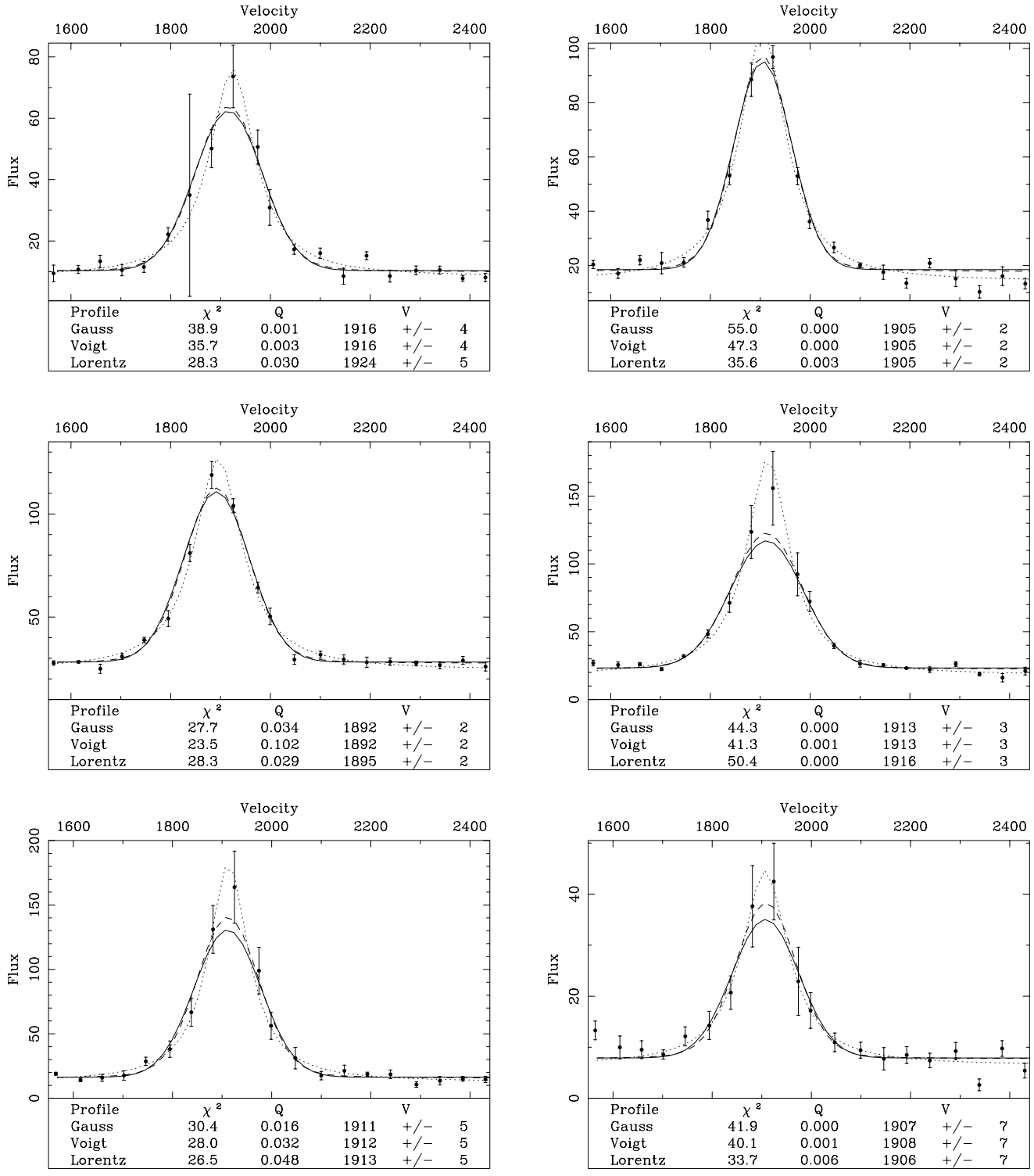

FIG. 2.—*Continued*

entzian, and four- and five-parameter Voigt functions. The results are shown in Figure 3 and were as expected. The Gaussian and four-parameter Voigt function gave essentially identical velocity fields. The full five-parameter Voigt function failed to converge or failed the (liberal) error cuts for the majority of the line profiles. And the Lorentzian fitted a larger number of profiles because of its tendency to peak high and make the flux cut where the others fail. But the small-scale structure is different, as this is skewed by the errors (as noted above). This foray into alternative fitting functions then provides a cautionary note that one needs to understand, in detail, the behavior of the fitting function in order to avoid introducing spurious errors, on various size scales, in the derived velocity fields. Although a Gaussian does underestimate the flux in the line, it seems to be the most free of these kinds of errors and thus provides the most robust measure of the velocity field, which is the principal item of interest. Since the four-parameter Voigt function does not provide a significantly better model of the line profile shape and the full five-parameter Voigt function

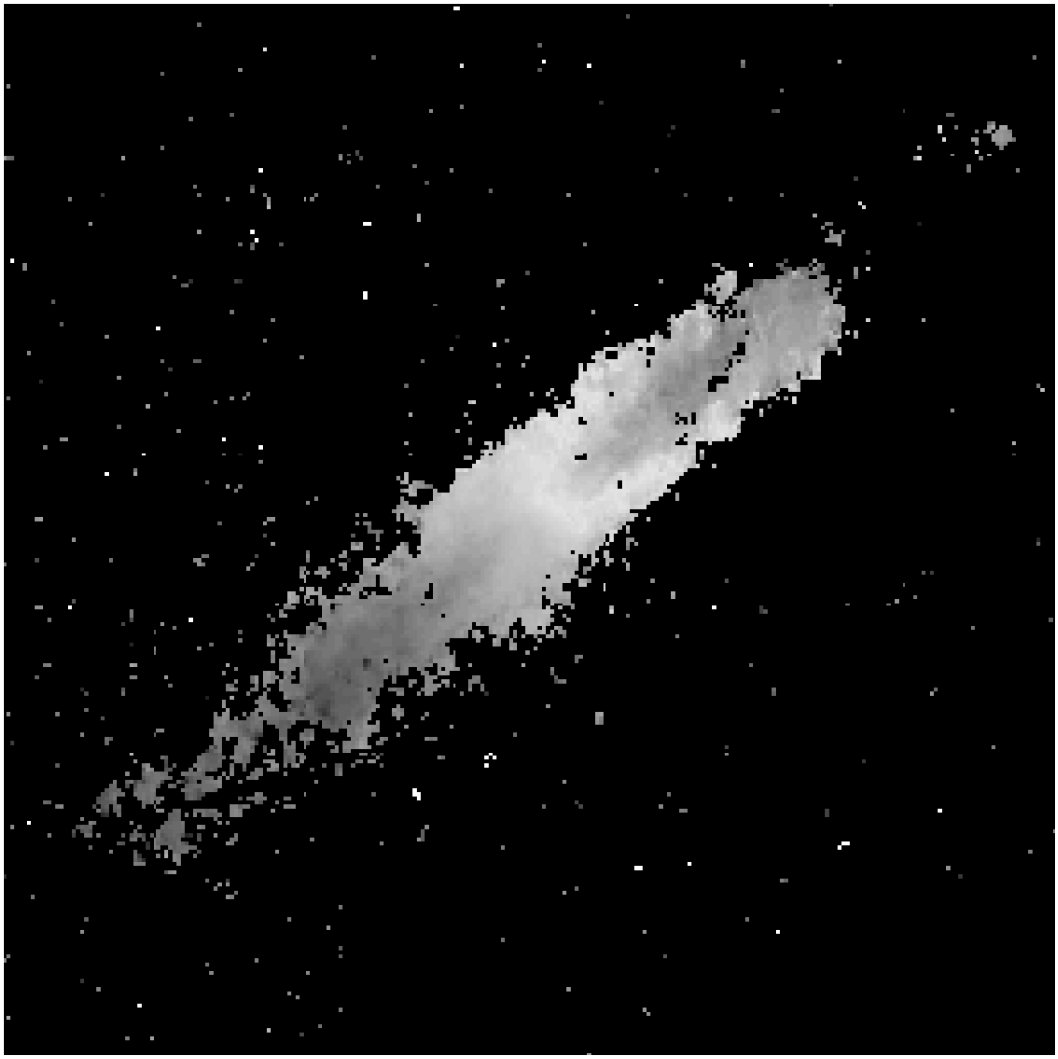

FIG. 3.—Velocity fields for E358 derived from Gaussian (*top left*), Lorentzian (*bottom left*), and four- (*top right*) and five-parameter Voigt (*bottom right*) functions.This is a gray-scale image; the full color images are available in the online edition of the Astrophysical Journal.

must be run interactively, we conclude that Gaussians should be used to fit Fabry-Perot line profiles and that a separate narrowband image should be taken for the most precise measure of Hα flux.

2.3. *Bimodal Line Profiles*

In most cases, line profiles were defined by a single peak. However, the data from NGC 1406 exhibited bimodal line profiles. Secondary peaks are expected if the gasdynamics becomes complicated when two separate dynamical structures are imaged by the same pixel. This can happen in expanding shells or in tidal tails of interacting galaxies (Mihos & Bothun 1997). Bimodal line profiles can be well modeled by summing two Gaussians as shown in Figure 4. On closer examination, all line profiles in NGC 1406 had a second peak one-sixth as high as the primary peak and separated by a distance of $\sim$600 km s^{-1}. The regularity of the separation and relative size of the two peaks over a large range of intensities argues against gasdynamics being the source of the second peak. Most likely the secondary peak is the [N II] λ6548. None of the other galaxies showed evidence of bimodal line profiles, perhaps indicating that [N II] λ6548 is unusually strong in this particular disk.

2.4. *Photometric Imaging Data*

To complement the FP data, we acquired, in photometric weather, images of the three highest angular size galaxies (E358, NGC 1292, and NGC 1406). *V*- and *I*-band images were taken using the CTIO 0.9 m telescope and standard filter set. Again, the images were processed in the usual way using standard IRAF tasks. The surface brightness profiles were obtained using the ellipse-fitting GASP software package described by Cornell et al. (1987). The zero-point calibrations were made using stars in Landolt standard fields (Landolt 1983). The surface brightness profiles are shown in Figure 5. These galaxies were a priori chosen to have little or no bulge component (verified by inspection of Fig. 5), so that any possible deviations from circular orbits should be driven entirely by the flattened dark matter halo (if it exists) and not by any bulge (or bar).

2.5. *Kinematic Modeling: The Tilted-Ring Model*

Since only line-of-sight velocities are observable, any attempt at using kinematic data to probe galaxy structure must deal with projection effects. The relevant coordinate systems are the sky (detector) coordinates (x, y, D), with D the distance from the galaxy to the observer, and a cylin-

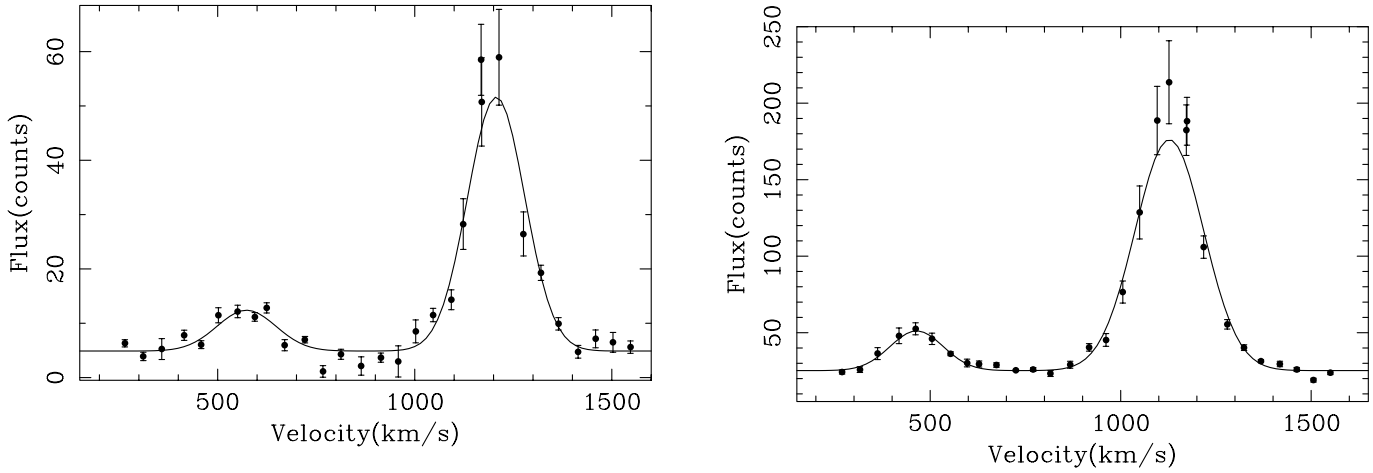

FIG. 4.—Sample bimodal line profiles fitted with a double Gaussian

drical coordinate system centered on the disk (R, ϕ, z). They are related by

$$\begin{pmatrix} x \\ y \\ D \end{pmatrix} = \begin{pmatrix} \cos\alpha & \sin\alpha & 0 \\ -\sin\alpha & \cos\alpha & 0 \\ 0 & 0 & 1 \end{pmatrix} \begin{pmatrix} 1 & 0 & 0 \\ 0 & \cos i & \sin i \\ 0 & -\sin i & \cos i \end{pmatrix} \times \begin{pmatrix} R\cos\phi \\ R\sin\phi \\ z \end{pmatrix} + \begin{pmatrix} x_0 \\ y_0 \\ D_0 \end{pmatrix},$$

with i the inclination of the disk to the LOS (for a face-on disk $i = 0$), α the position angle (P.A.) of the high velocity end of the galaxy on the detector, and ϕ measured from the P.A. This gives an observed LOS velocity of

$$v_{\rm LOS} = v_{\rm sys} + v_c(R,\phi)\cos\phi\sin i + v_s(R,\phi)\sin\phi\sin i + v_z(R,\phi)\cos i\,,$$

where $v_{\rm sys}$ is the LOS systemic (recessional) velocity of the galaxy, v_c is the circular velocity in the ϕ-direction, v_s is the

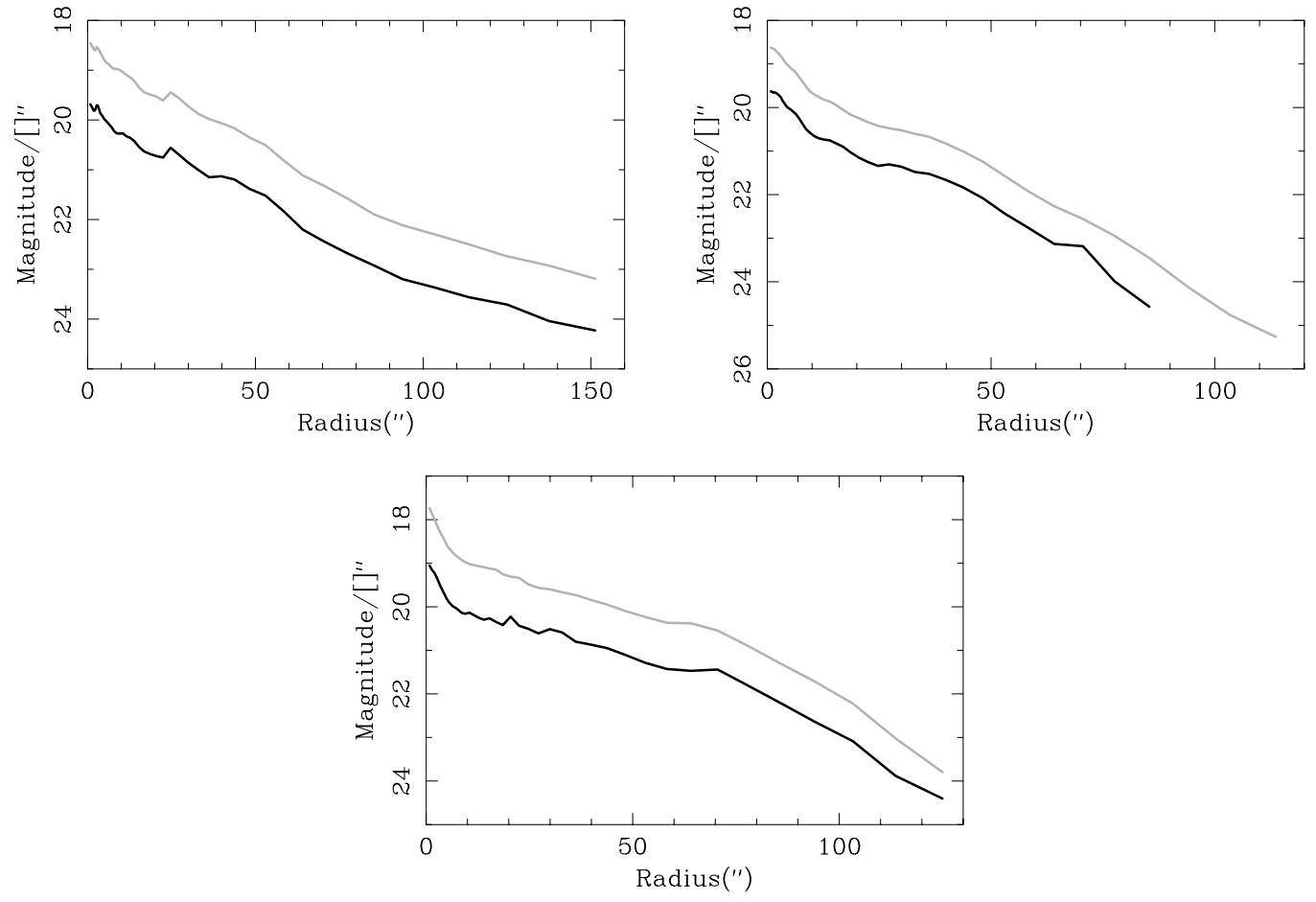

FIG. 5.—Calibrated surface brightness profiles for E358, N1292, and N1406. V band (*black*) and I band (*gray*)

radial (streaming) velocity, and v_z represents any infall/outflow motions.

The standard method for deprojecting galaxies from kinematic data is to assume that the galaxy is made up of a number of rotating solid body annuli, the tilted-ring model. The velocity field is fitted with the equation $v_{\rm LOS} = v_{\rm sys} + v_c \cos\phi \sin i$ for five free parameters: the center x_0 and y_0, the position angle (P.A.) α and inclination i, and the rotational speed v_c. The systemic velocity, $v_{\rm sys}$, was held fixed during the fit. The annular fits smooth both radially and azimuthally, which minimizes the influences of randomly distributed noncircular motions. (Systematic deviations from circular motions are more insidious and harder to deal with and are discussed later.) In spite of the smoothing, the radial distribution of recovered parameters showed rapid fluctuations about more slowly changing values. This was found to be an artifact of the fitting algorithm; changing the parameters changed which pixels were contained in the annulus, causing a slight degeneracy in the parameters. This was dealt with in two ways. First, rather than the common least-squares minimization, the rms deviation was minimized instead. This encouraged the fitted algorithm to choose a better balance between a small least-squares value and keeping a large number of pixels in each annulus, since the least-squares value is minimal (zero) when there are no pixels in the annulus. This improved the performance, though there was still a degeneracy near the minimum rms value. To remove the remaining fluctuations, the parameter distributions were lightly smoothed (on a smaller scale than the annular width) after the fit was complete. Near the edge of the velocity fields, the data become sparse and the fits eventually failed, leading to a maximum radius to which the tilted-ring model could be extended, so they were truncated at that point. The final step of the procedure was to project the annuli back onto the sky and obtain a predicted value for $v_{\rm LOS}$at each point, giving model images which could be compared directly to the velocity fields of galaxies. The generation of these model images will later allow us to add random noise to compare to real images in order to assess the overall amplitude of rms disturbances in the disk velocity field.

2.6. *The Pre-Fit*

Since the systemic velocity represents the bulk motion of a galaxy, it should not vary between annuli, and there are theoretical reasons to expect gas orbits to be concentric so that the center should not be allowed to vary either. SBWM allow both to vary in their kinematic disk fits, which would be acceptable if the parameters only varied a little. For some galaxies, however, the difference in systemic velocity between annuli can be as high as 30 km s^{-1}. This large a shift in $v_{\rm sys}$ seems artificial but can have a large impact on the other parameters, especially the position of the center which is directly linked to $v_{\rm sys}$. On the other hand, we are using emission lines as a diagnostic, and it is well known that emission lines are a poor tracer of the systematic velocity. Hence, shifts between annulus could occur if say, kinematic feedback to the gas from star formation, has caused a significant noncircular motion at some radius. At some level it is difficult to assess the reality of these apparent shifts and whether or not they are mostly due to the fitting procedure or are a real asymmetry in the velocity distribution of the emission line gas.

TABLE 2

PRE-FIT VALUES FROM TEST VF

Level (1)	x_c (arcsec) (2)	y_c (arcsec) (3)	$v_{\rm sys}$ (km s^{-1}) (4)
0.....	110.5	109.0	1369
5.....	109.9	108.9	1371
10.....	109.7	108.9	1372
15.....	109.4	108.5	1373
20.....	109.3	108.4	1374

To determine the systemic velocity and the position of the center, the entire velocity field was fitted as a single solid-body disk with the geometric parameters (x_0, y_0, α, i) allowed to vary. This method was chosen because in many galaxies the gas is distributed asymmetrically. Performing an initial fit and taking the average $v_{\rm sys}$ was rejected because certain pixels are in multiple annuli, making it difficult to obtain a proper weighting. The single-disk method finds the point about which the cos ϕ term is minimized for the entire velocity field. This should give a good estimate. It also insures the proper connection between the choice of center and the systemic velocity.

The pre-fit procedure was tested on the same artificial velocity fields used to test the tilted-ring model (see next section). Small amounts (from 5 to 20 km s^{-1}) of velocity structure were added in the artificial velocity field (generated using NGC 1292 as a model) at various radial locations to determine the extent to which this changed the geometric center of the ring and/or the systemic velocity (see Fig. 6). Table 2 shows that the added structure had little effect on the center estimate and the systemic velocity. Another check of the pre-fit procedure is to compare the systemic velocities obtained to the accepted values of the heliocentric velocities of the galaxies in the sample, taken from the NASA Extragalactic Database. This comparison is given in Table 3. These systemic velocities are generally from 21 cm measurements but are sometimes absorption (opt) or emission (Hα) line measurements. This is so noted in column (3) of Table 3. We estimate that the systemic velocities derived from the tilted-ring model method are accurate to 5–15 km s^{-1}, and hence the agreement with the other data is reasonable. The only case which is cause for some concern is that of NGC 3463. Giovanelli et al. (1997) measure a 21 cm velocity of 3989 $\pm$ 5 while the NED velocity, based on Hα measurements is 3950 $\pm$ 10. Our value of 3917 $\pm$ 15 km s^{-1} is significantly lower. In this case, its very likely that the emission line velocity is not acting as a good tracer of the systemic velocity. Overall, however, our results

TABLE 3

VELOCITY COMPARISON

Galaxy Name (1)	$V_{\rm hel}$ (km s^{-1}) (2)	$v_{\rm sys}$ (km s^{-1}) (3)
ESO 358–G63.....	1932	1950
ESO 437–G30.....	3759	3732
NGC 1292.....	1367	1368
NGC 1406.....	1075	1066
NGC 2417.....	3184	3175
NGC 3463.....	3950	3917
IC 2559	2974	2955

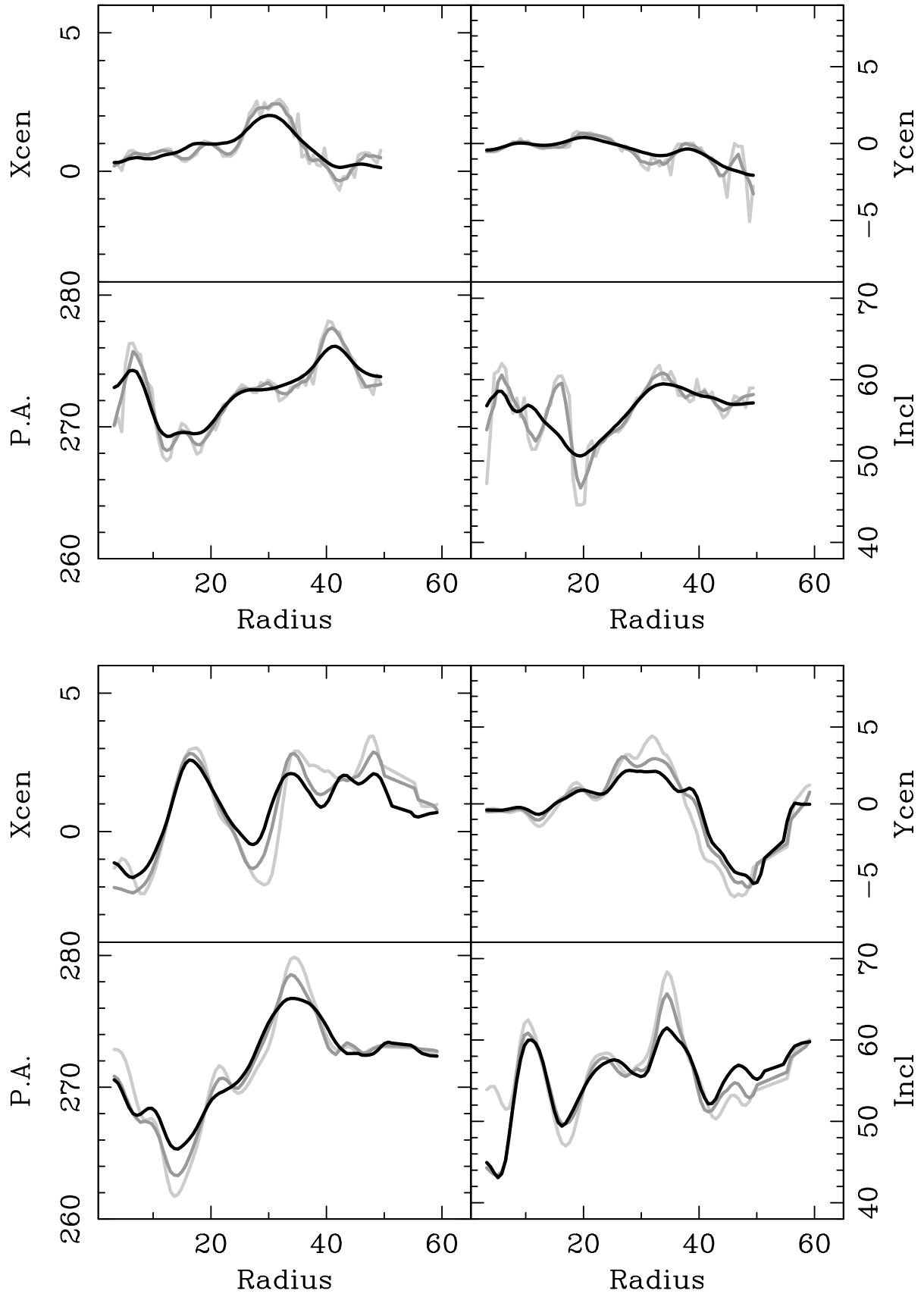

FIG. 6.—Disk parameters recovered from test velocity fields. (*Top*) Parameters before final smoothing (*light gray*), after final smoothing (*dark gray*), and recovered from test velocity field with no structure (*black*). (*Bottom*) Parameters recovered from test velocity field with 10 (*black*), 15 (*dark gray*), and 20 km s^{-1} (*light gray*) rms structure levels. Linear units measured in arcseconds and angles measured in degrees.

are consistent with those of SBWM, who also find similar good agreement between 21 cm systemic velocities and those obtained via the tilted-ring model.

3. TWO DIMENSIONAL VELOCITY FIELDS IN SPIRAL GALAXIES

3.1. *Testing the Tilted-Ring Model*

The tilted-ring model can be used to construct a velocity field from which a rotation curve can be extracted. In addition, the tilted-ring model provides the mechanism to detect possible noncircular motions in these disks. But how well can the method work? To determine the ability of the tilted-ring model to accurately recover the structure of galactic disks from real velocity fields, an artificial velocity field was generated for a disk with known parameters. To create another test velocity field with parameters that mimic those found in real disks, N1292 was modeled, and the resulting parameters used to build the test velocity field. The test velocity field was fitted with a tilted-ring model, and the parameters are shown in Figure 6. They are nearly identical to those used in the construction of the test velocity field but give an indication of the radial smoothing due to the finite annular widths.

Real velocity fields contain noncircular motions which were removed from the test velocity field by the smoothing in the tilted-ring model procedure. To examine the effects noncircular motions have on the parameter determinations, they were simulated by producing an image of Gaussian noise which was smoothed until its structure resembled that seen in the real velocity field of N1292. This was then scaled to rms levels of 5, 10, and 15 km s^{-1} and added to the test velocity field. The resulting images were then modeled in turn, and the recovered parameters are shown in Figure 7. These generally followed those obtained from the test velocity field without the added small-scale structure, but the size of the deviations was found to scale with the size of the structure. The noncircular motions thus have a small but noticeable influence on the derived parameters, typically 2″ on the center and 3° on the orientation angles. This effect is most evident at large radii ($R \geq 50''$) where the outer edge of the annulus passes the edge of the test velocity field's disk. In real galaxies the data normally become increasingly sparse with radius, so this truncation effect should not be apparent. Visual comparison of the test velocity field images shown in Figure 7 indicates that the noncircular motions in N1292 are $\sim$10 km s^{-1}, typical of the galaxies studied (see § 4).

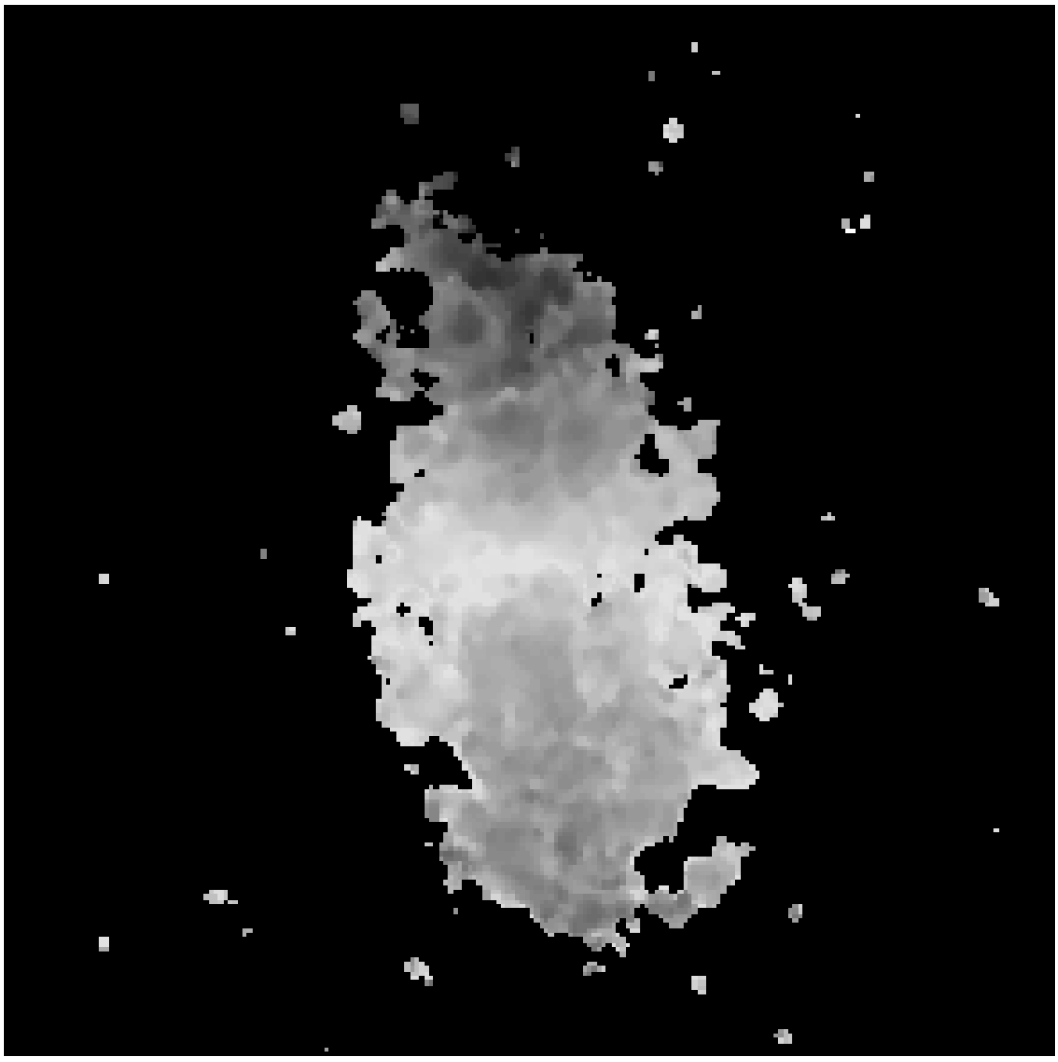

FIG. 7.—Test velocity fields. Shown are (*left to right, top to bottom*) the real velocity field of N1292, and the test velocity fields with small-scale structure of 5, 10, and 15 km s^{-1}. This is a gray-scale image; the full color images are available in the online edition of the Astrophysical Journal.

3.2. *Centering and Inclination Issues*

The measurement of the disk galaxy inclination, however, can be a tricky procedure. SBWM have called attention to the rather large scatter that results in the comparison of photometric versus kinematically determined inclinations (see also Sakai et al. 1999). This is a matter of some concern in the practical application of the TF relation. In some cases, the scatter is caused by a slight difference between the photometric and kinematic centers of the galaxies. This effect could even be real if the light distribution does not exactly trace the mass distribution in the inner parts of disk galaxies. The submaximal disk hypothesis of Courteau and Rix would suggest that such a center mismatch could occur. For E358, N1292, and N1406 in our sample it is possible to obtain a photometric estimate of the center. The photometric center of a galaxy is taken as the average center at large radii. While photometric data extend much past the optical kinematic data, and so may be susceptible to warps, etc., the kinematic and photometric estimates are nearly identical. Only for E358 is the difference appreciable—5″.5 (=410 pc). This made a 12 km s^{-1} lowering of the systemic velocity necessary when using the photometric center in the tilted-ring model, which places it farther from the rather accurately determined published heliocentric velocity.

While the center is expected to be constant, during the testing of the tilted-ring model process it was allowed to vary. This was done for two reasons. The first is that allowing the center to vary resulted in more complicated parameter sets and thus provided a more rigorous test of the tilted-ring model. The second was to compare the kinematic parameters to those found during the ellipse fitting in the photometric reductions. The kinematic and photometric parameters are plotted in Figure 8. While the agreement is not spectacular, the parameters share many of the same trends and possess similar features. On large scales, this indicates a relatively tight connection between the distributions of light and mass. The small-scale noise, however, may represent features in the light distribution that are able to generate local noncircular motions. This is one of the primary results we are interested in obtaining, and it will be more fully discussed in § 4. For now, Figure 8 should be viewed as an affirmation of the more global results obtained by SBWM that the correlation between the photometric and kinematic structure of disk galaxies is noisy. Inspection of Figure 8 shows that the inclination profiles are fairly noisy and often have "features" in them. These features may be due to the influences of noncircular motions at certain radii (e.g., streaming motions). At the very least, the inclination profiles, coupled with the global comparison of SWBM strongly suggests that inclination measures of disk galaxies are not particularly robust unless they are very edge-on.

In the case of NGC 1292, there seems to be poor alignment between the kinematic and photometric determinations of P.A. in the inner regions of the galaxy. In particular, there is a mean difference of approximately 10° in the inner 30″. The reason for this misalignment is not at all clear but it again does raise the issue of what is the best tracer of the P.A. (and inclination) of a disk. Certainly, the emission line velocity field is measuring a much different component of the stellar population than *I*-band photometry. The relatively good agreement between the *V*- and *I*-band observations, compared to the kinematic data, to first order suggest that the underlying stellar population defines a different P.A. than the emission line gas that is ionized by the very youngest population. The small misalignment observed here could result from (a) inadequate sampling of the velocity field in the inner regions (this seems unlikely), (b) kinematic feedback from star formation which has disturbed the emission line gas, or (c) an asymmetric distribution of star formation (most likely). This suggests that photometric tracers provide more reliable indications of disk P.A. and inclination.

Choice of center, however, appears to be far less problematical than the determination of the inclination. Recall that the center of the velocity field can be chosen either by using the center of symmetry of the tilted rings (the kinematic center) or by using the optical isophotes (the photometric center). In addition, we have also allowed the center to become a fitting parameter of the tilted-ring model (the variable center). All three center estimates (kinematic, photometric, and variable) gave tilted-ring model's that reproduce the observed velocity fields equally well. No simple statistical test showed one model as better than the others, since the true rotational structure is masked by the noncircular motions. Thus, models were created using all three and the radial profiles of P.A., inclination, and *X* and *Y* pixel centroid are shown in Figure 9. Overall, the choice of center had little effect on the P.A. or the inclination, so the structure exhibited by them is likely to be real. In the variable center model, the centers show shifts of $\sim$300 pc. As discussed in Paper II, this shift has a significant impact on the robustness of the extracted rotation curve. Many of the galaxies show the largest center shift at large *R*, which may indicate a physical misalignment of the inner and outer disk rotation axes. Two galaxies, N1292 and E437, show signs of significant misalignment between inner and outer disk position angles.

3.3. *The Velocity Fields*

The velocity fields that have been derived for our sample galaxies from Fabry-Perot data cube line profiles fitted with Gaussians are shown in Figure 10. As the velocity fields predicted by the models with the different centers are all similar in appearance, only the variable-center models are shown here. Of course, velocity fields presented in gray scale have limited information and we cannot afford to publish color images. We encourage the reader to see the color images available in the online edition of the Astrophysical Journal.

In Figure 10, all aspects of the data and the data reduction are shown. The top row shows the continuum, intensity and dispersion maps which we do not generally make use of in this paper. The bottom row shows the velocity field, the model velocity field which is reconstructed from the tilted-ring model fits, and the residual velocity map obtained by comparing the model with the data. It is with this residual map that we can estimate the rms noise in the velocity field in a given galaxy. We discuss this in detail below. Here we give some brief comments on the individual galaxies in our sample. The reader may wish to confirm these through an examination of the color images available in the online edition of the Astrophysical Journal.

E358.—This fairly inclined disk galaxy is quite well sampled at Hα. The intensity map reveals significant star formation in the inner regions (including the nucleus) and more star formation on the leading side than the trailing

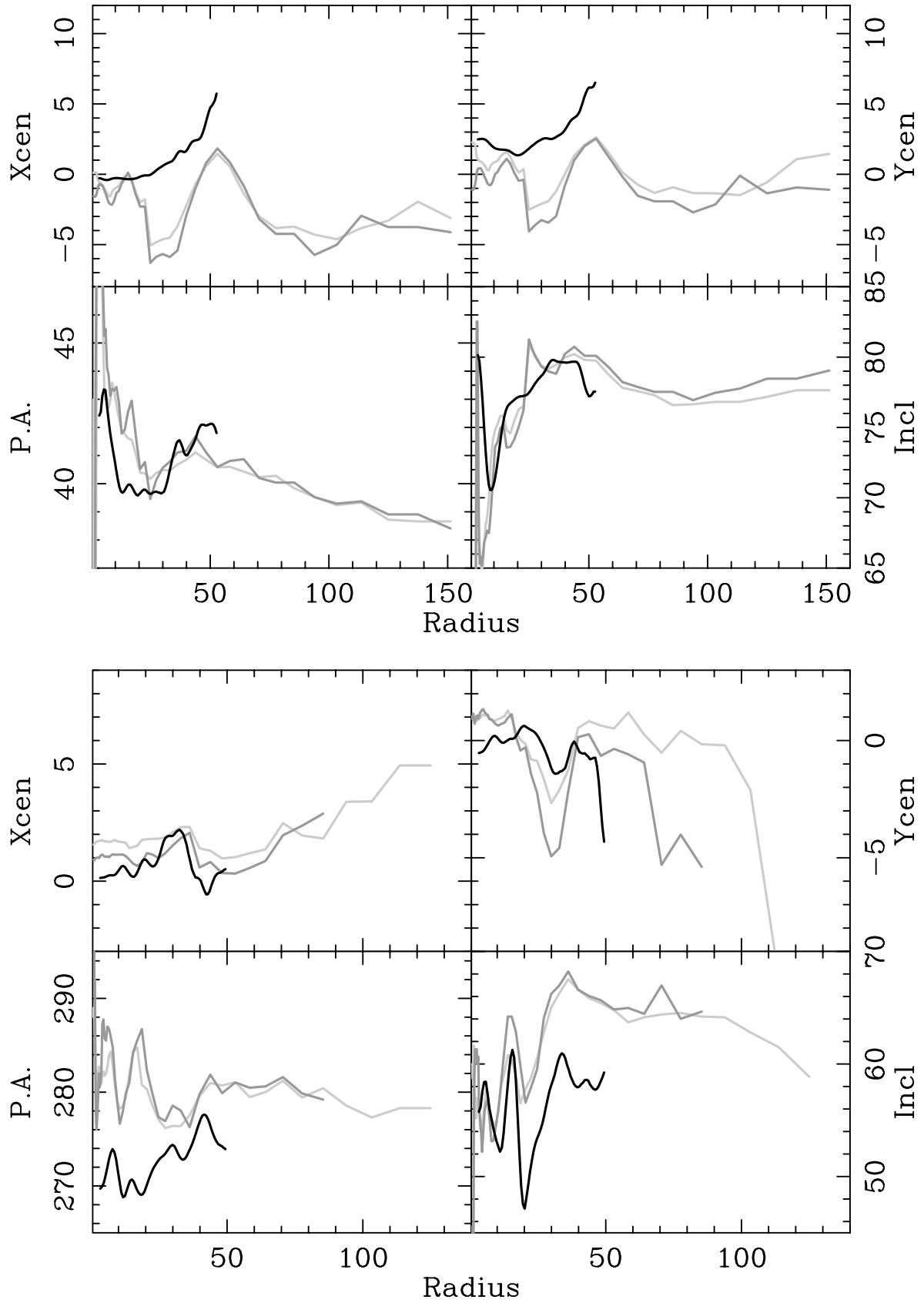

FIG. 8.—Kinematic and photometric disk parameters for E358, N1292, and N1406. Kinematic parameters (*black*), and *V* band (*dark gray*) and *I* band (*light gray*) photometric parameters. Linear units measured in arcseconds and angles in degrees.

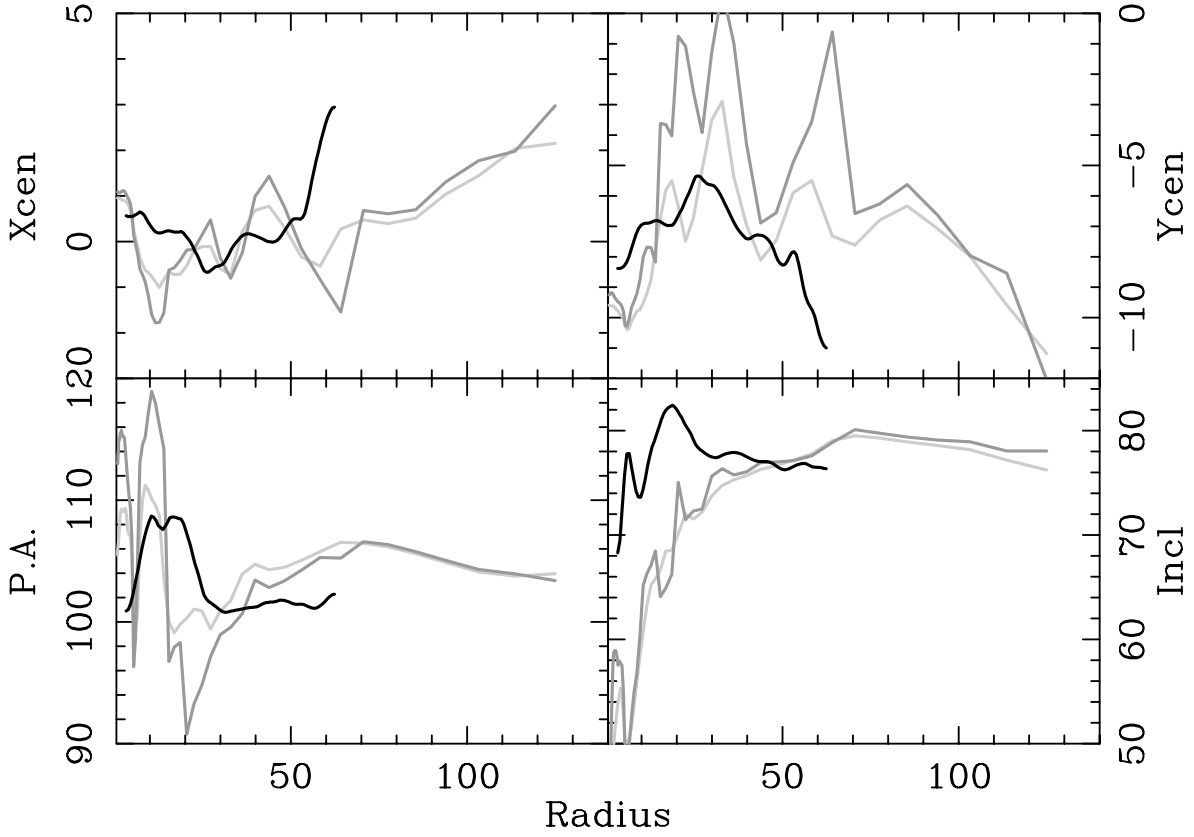

FIG. 8.—*Continued*

side. The velocity field is very well sampled, and a detached region of Hα emission can be clearly seen in both the intensity and velocity maps.

N1292.—This galaxy is extraordinary in the amount of diffuse Hα that is present (analyzed in more detail in Paper III). There are only a few prominent H II region complexes and the nucleus is not particularly strong. As a result of the distributed diffuse Hα, the velocity field is very well sampled.

N1406.—This is also a fairly inclined disk. The star formation activity is primarily limited to the inner disk and would appear to define two spiral arms. The trailing side of the galaxy exhibits a discontinuity in the velocity field coverage due to a break in Hα emission from the disk.

E437.—This fairly inclined disk has relatively spotty coverage in the outer parts of both ends of the disk. The bulk of the Hα emission is confined to large complexes in the inner disk and on the leading edge. The trailing edge has no large Hα emitting complexes except for one at the very end of the disk.

N2417.—This late-type spiral clearly shows Hα emission strongly confined to multiple spiral arms. Unlike the case of NGC 1292, there is not a pervasive diffuse component to the Hα emission. As a result, the velocity field is relatively sparsely sampled and there is little Hα emitting gas at the velocity endpoints of the rotation curve. Comparison of the velocity field image with the continuum image immediately shows some of the difference that exist between photometric and kinematic inclinations and position angles.

N3463.—This is the only galaxy in the sample of seven that shows evidence for a ringlike structure of star formation. A very bright Hα emitting region can be seen to the North of the nucleus. The nucleus itself has no Hα emission. This somewhat asymmetric emission line structure may therefore account for the order 50 km s^{-1} difference between the Hα and 21 cm systemic velocities. Like E358, a detached region of star formation is present in both the intensity and velocity maps. The velocity field is very well sampled in this case, except for a hole in the southern (leading) end of the disk.

IC 2559.—This relatively small galaxy has an unusual distribution of star formation which is heavily confined to the inner regions. The overall distribution of star formation is fairly asymmetric but the velocity field appears quite regular and well sampled.

3.4. *Residual Velocity Fields*

While rotation accounts for the bulk of the motions in disk galaxies, noncircular motions are present as well. The residual velocity is the difference between the observed LOS velocity and that expected due to rotation. Thus, the residual velocity is positive where the LOS velocity exceeds the predicted value and negative where it falls short. Maps of the residual velocities, often called residual velocity fields, were obtained for each galaxy by subtracting the model velocity field from the true velocity field and are shown in the bottom right panel for each galaxy in Figure 10. Because the residual velocity field depends on the predicted rotation, careful construction of the tilted-ring model is crucial and we have again used the variable-center model to produce the residual velocity field.

Earlier we displayed the test model velocity field, with noise added, for NGC 1292 as a check on the tilted-ring model (see Fig. 7). The same procedure was done for all the

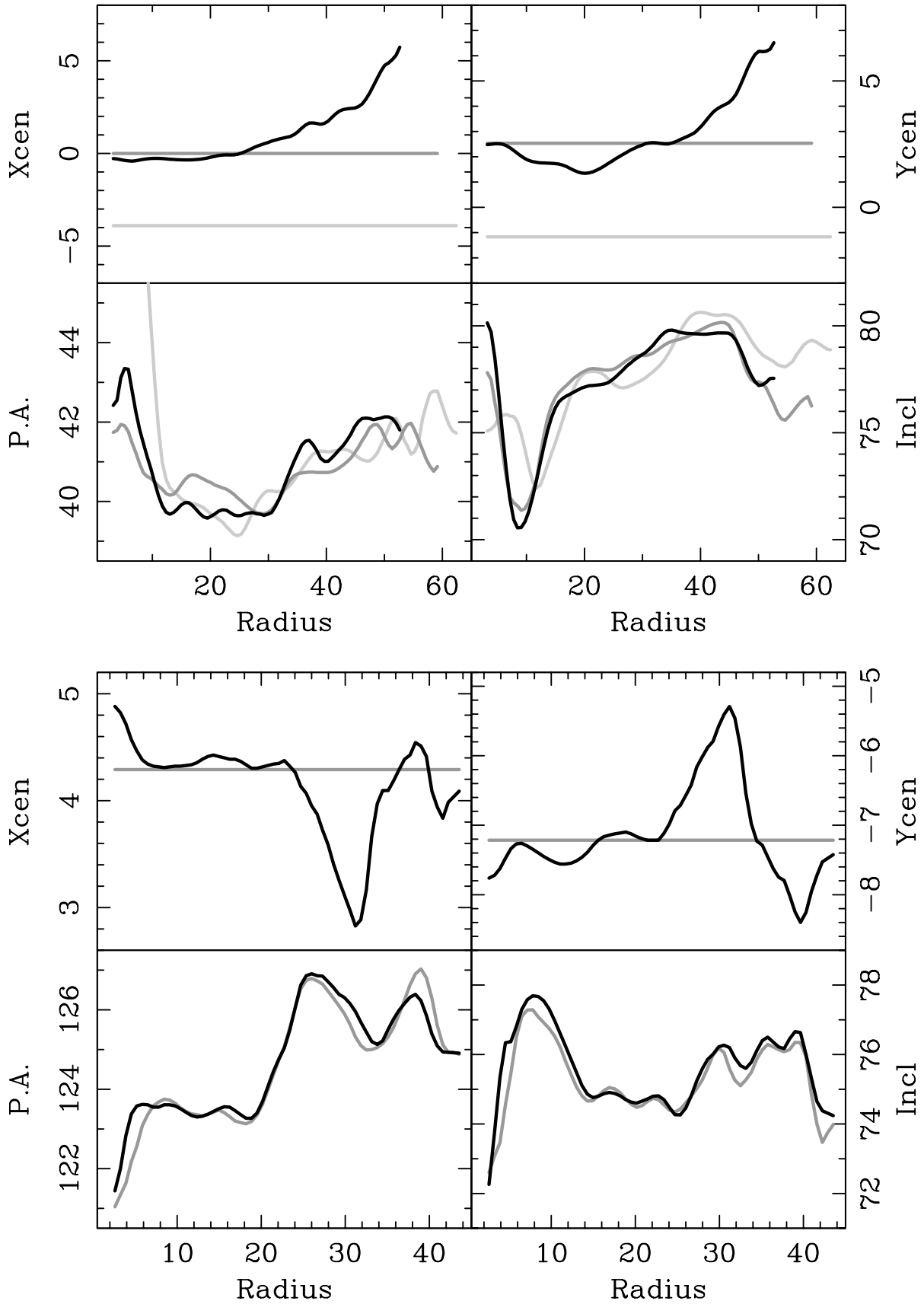

FIG. 9.—Model disk parameters for E358, N1292, and N1406. Second page is for E437, N2417, and N3463. Parameters from variable center (*black*), from kinematic center (*dark gray*), and photometric center (*light gray*). Linear units measured in arcseconds and angles measured in degrees.

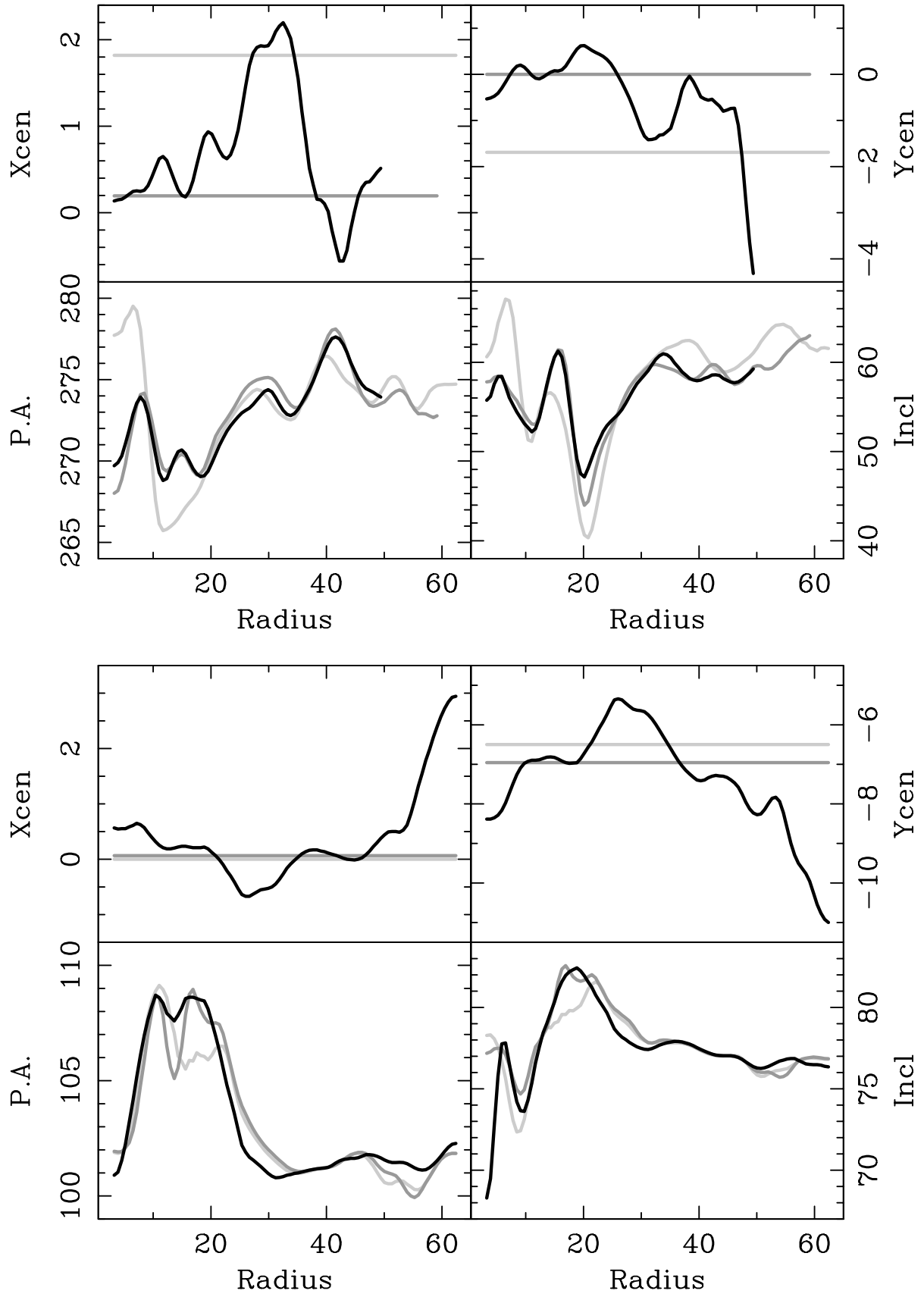

FIG. 9.—*Continued*

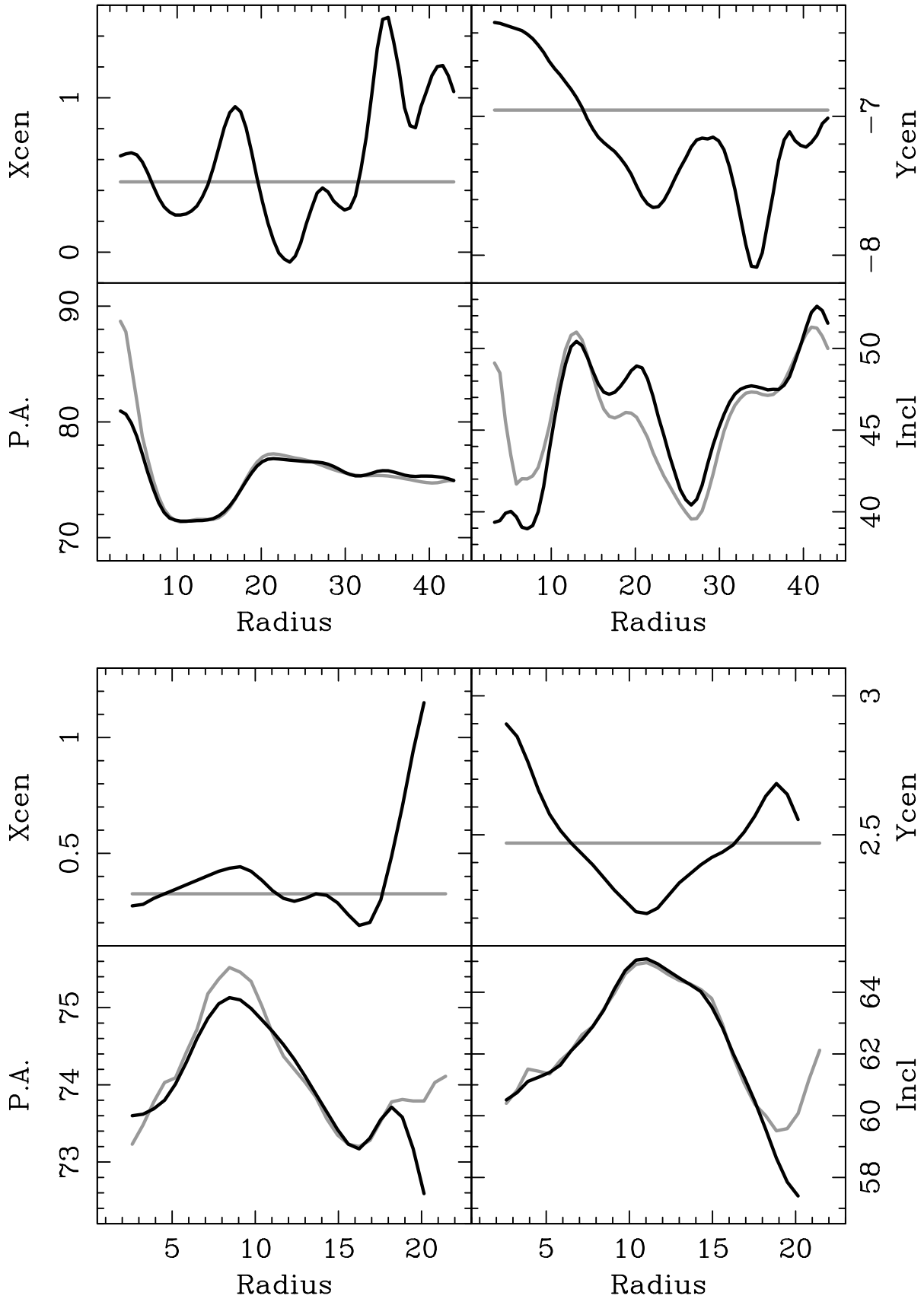

FIG. 9.—*Continued*

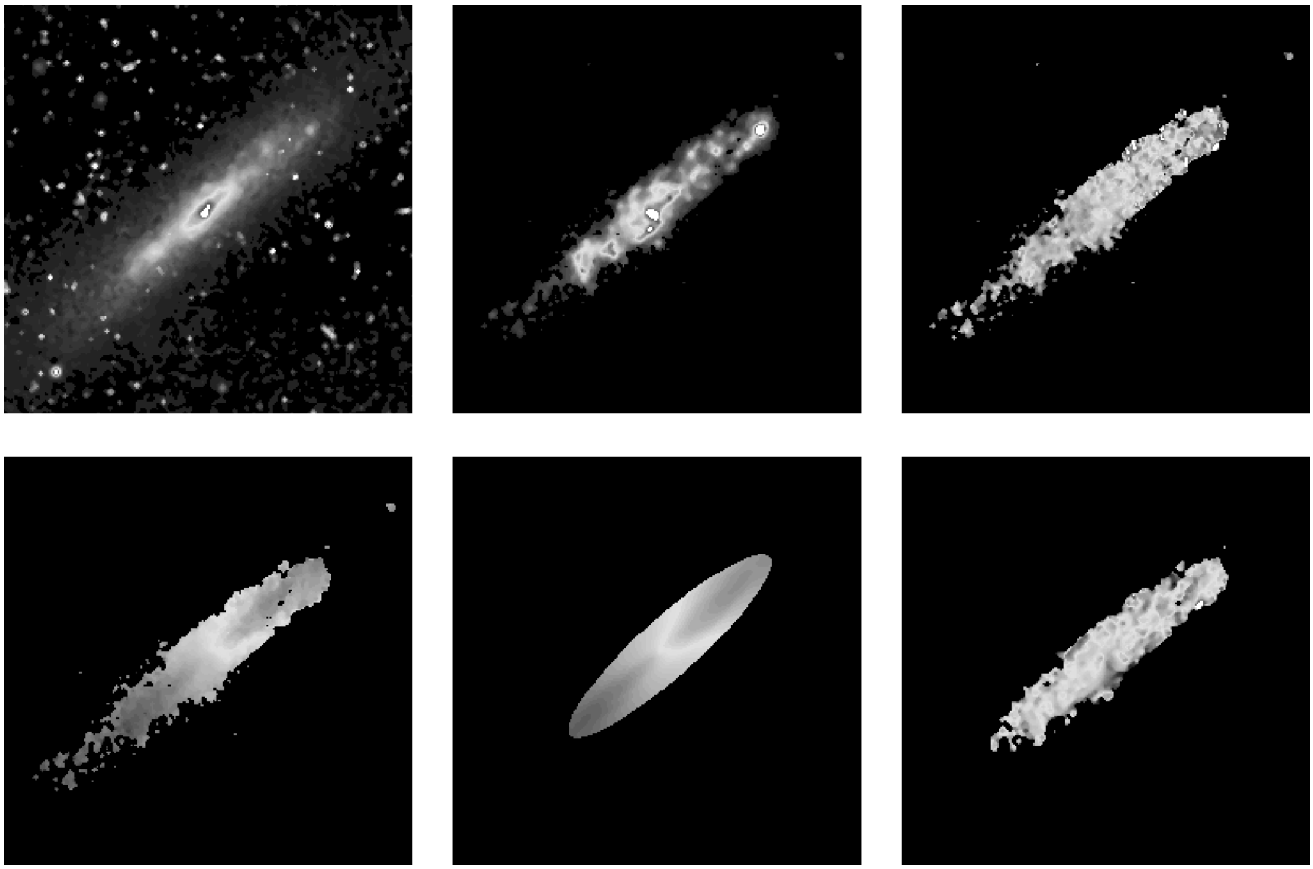

FIG. 10.—Color images of the velocity fields for the seven sample galaxies. In order, the galaxies shown are E358, N1292, N1406, E437, N2417, N3463, and I2559. In each figure the top row shows the continuum, intensity, and dispersion maps, and the bottom row shows the velocity field, the model velocity field, and the residual velocity filed. This is a gray-scale image; the full color images are available in the online edition of the Astrophysical Journal.

other galaxies in the sample and, the results were the same as seen for NGC 1292. In general, by comparing the models with noise to the data we find that the average size of the residual velocity is $\sim$10–15 km s^{-1}. This agrees with well with the amplitudes of the bumps and wiggles noticed in the FP rotation curves obtained by SBWM and also by us in Paper II. The residual velocity fields show none of the systematic patterns that would indicate that the tilted-ring model parameters are incorrect (Athanassoula 1984), although there is some evidence of radial motion, particularly in the case of NGC 1406. The residual velocity fields, in general, do not show large-scale features or much asymmetry. This strongly suggests that the velocity field of a typical disk galaxy is adequately described by the tilted-ring model upon which 10–15 km s^{-1} of Gaussian noise, due to noncircular motions, is sprinkled. At local places in the disk, these noncircular motions could be of larger amplitude, but globally averaged, our data suggest an rms value of 10–15 km s^{-1}. This is good for the TF relation as it suggests the velocity fields in most spiral galaxies are quiescent, a point which is clearly consistent with the observed scatter in most TF samples.

3.5. *Possible Sources of Residual Velocities*

3.5.1. *Kinematic Feedback from Star Formation*

One of the principal attributes of spiral arm density wave theory (e.g., Yuan & Cheng 1989) is the production of streaming motions by the spiral structure itself. There is ample evidence, from 21 cm mapping of the Galaxy, that this is occurring at the $\sim$10 km s^{-1} level. To the extent that our data confirm this, we are not concerned with further elucidation of this source of noncircular motions but instead focus on other sources that hitherto have not been strongly considered. Indeed, many processes that can produce residual velocities also have other observable effects. For example, regions of intense star formation are easily seen in the Hα intensity image and turbulent motions in those regions may lead to an increase in the local velocity dispersion. Thus, correlations may exist between the residual velocity field and the features in the intensity and dispersion maps. At some level, kinematic feedback to gas from the process of star formation must be important. Clearly, in the case of low mass irregular galaxies, this feedback may well be the major factor in determining evolutionary history as, in extreme cases, significant winds can be generated which can blow the gas to large distances (e.g., Devost, Roy, & Drissen 1997; Martin & Kern 1999; see also Martin 1997). The situation in normal spiral galaxies has not been scrutinized yet, but our data allow for a preliminary investigation.

To look for the signature of kinematic feedback to the gas from star formation, contours of constant residual velocity were plotted over gray-scale images of the intensity and dispersion features, and vice versa. This may seem redundant, but because the contour levels were chosen somewhat arbitrarily, correlations are sometimes more visible in one plot than the other. To create maps of just the intensity and dispersion features, the images were boxcar

averaged to create background images which were then subtracted from the originals. The relevant images are shown in Figure 11. As is apparent, not all regions of large residual velocity are associated with an intensity or dispersion feature, and neither are all intensity and dispersion features related to large residual velocities, but there are obviously some correlations. These can be seen as the straightforward tracing of a gray-scale feature by a contour, while in other areas a contour may avoid a feature. The intensity and dispersion correlate equally well with both positive or negative residual velocities and the correlation between the residual velocity field and velocity dispersion is slightly stronger than between the residual velocity field and the Hα intensity for most galaxies. There are few instances where the same residual velocity correlates with both the intensity and dispersion.

In general, the correlations with are found are on relatively small spatial scales (e.g., 0.5–1 kpc), which is consistent with the idea that many velocity residuals arise from to local causes, such as star formation. Of course, in many cases star formation is coincident with strong spiral structure and the kinematic feedback may be secondary to the spiral density waves in producing the observed residual velocities. On the other hand, galaxies with multiple but weak spiral structure like NGC 2147 have residual velocities of the same amplitude as those observed in disks with stronger spiral structure (e.g., NGC 1292). This would suggest that the residual velocities can be driven by the local star formation rate. Because the dispersion maps are generally noisy, it is difficult to determine if the overall velocity dispersion of the Hα emitting gas, on scales of a few kpc, is affected by enhanced star formation. The use of a narrow etalon would be required to make a better assessment, but this would be an extremely time-consuming observation per galaxy.

3.5.2. *Triaxial Potentials*

Another possible source of residual velocities, albeit operative over a larger spatial scale, would be related to the failure of the tilted-ring model to adequately describe the

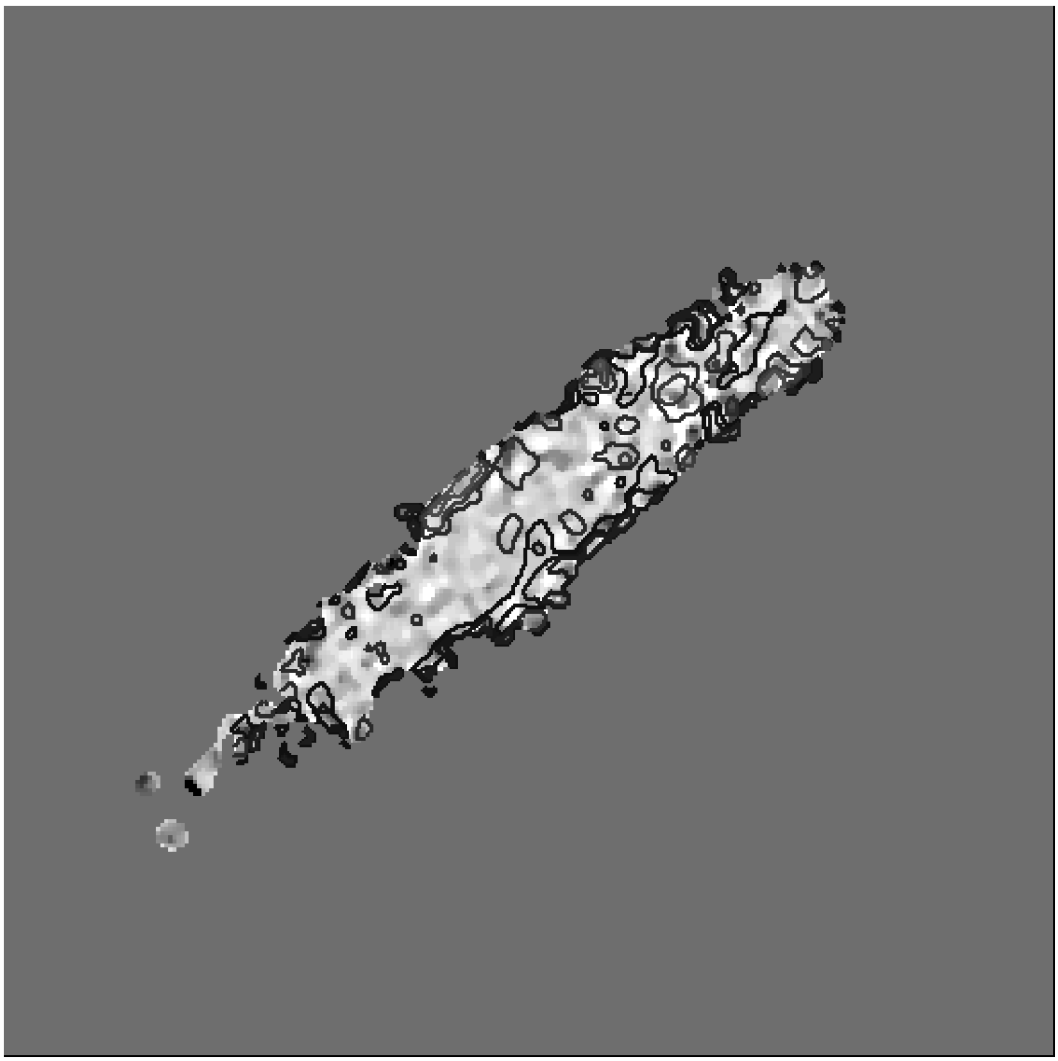

FIG. 11.—Correlation of residual velocities with intensity and dispersion images. Shown are residual velocity contours over intensity feature gray-scale (*top left*) and over velocity dispersion feature gray-scale (*bottom left*), and intensity (*top right*) and dispersion (*bottom right*) contours over gray-scale of residual velocity fields. The galaxies displayed here are E358, E437, N1292, N1406, N2417, and N3463. This is a gray-scale image; the full color images are available in the online edition of the Astrophysical Journal.

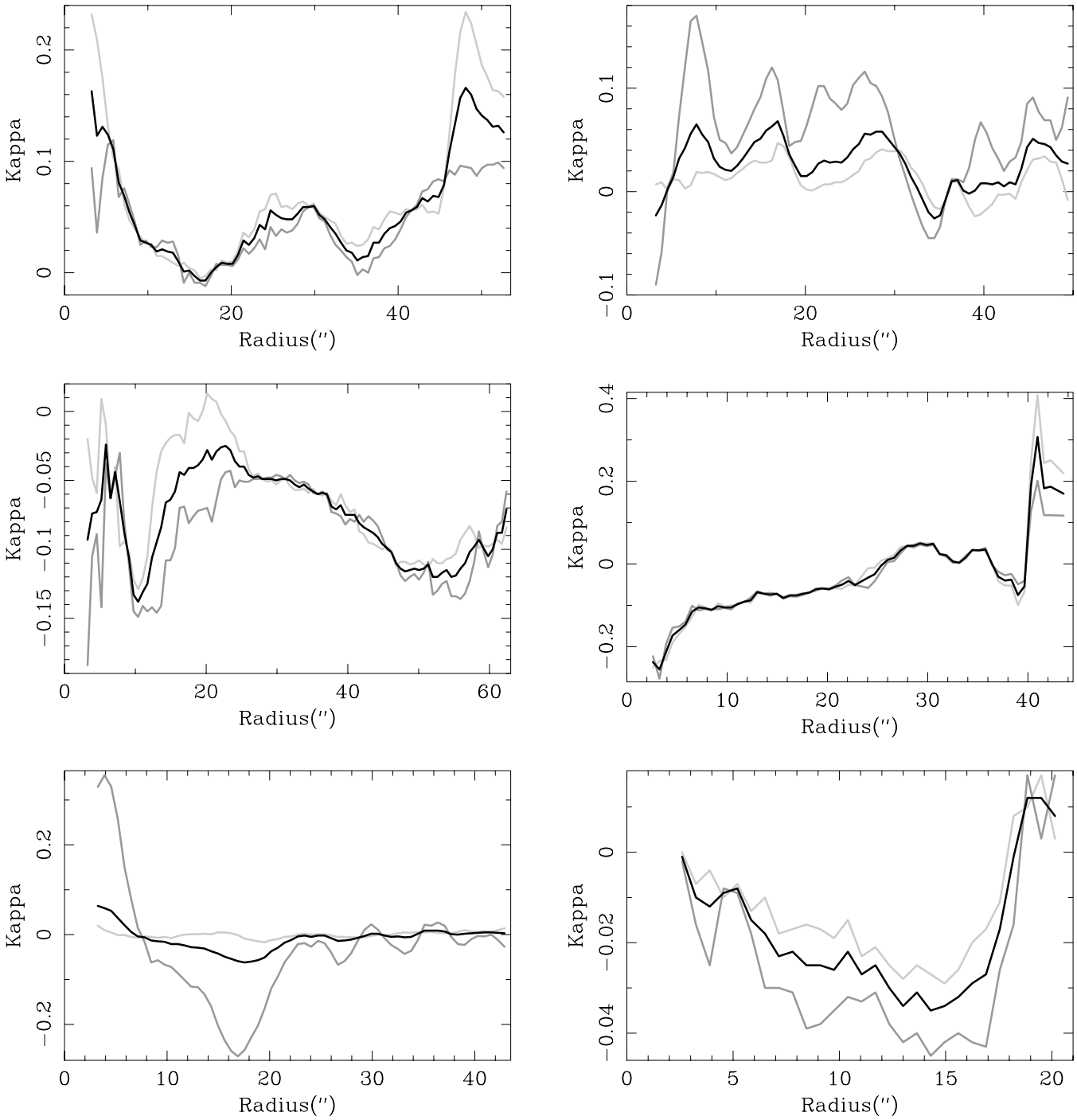

FIG. 12.—Plots of $\kappa = \ell \sin 2\phi_{obs}$ for E358, N1292, N1406, E437, N2417, and N3463

TABLE 4

MEAN VALUES OF κ

Galaxy Name	κ
ESO 358–G63.....	0.035
ESO 437–G30.....	−0.034
NGC 1292.....	0.032
NGC 1406.....	−0.079
NGC 2417.....	0.005
NGC 3463.....	0.019

orbital motions of the gas. As mentioned in the introduction, there is the possibility that disk galaxies are embedded in triaxial rather than axisymmetric potentials. A triaxial potential has a preferred axis which drives elliptical gas orbits whose eccentricity is determined by the aspect ratio of the three principal axes. Potentially, these elliptical orbits could be present at any radius.

As is well known from isophotal fitting, approximating an elliptical distribution with one that is circular introduces a regular pattern of angular harmonics (Jedrzejewski 1987).

The residual velocities at each R (i.e., in a given annulus of the tilted-ring model) should satisfy

$$\delta v = v_c \sin i \left[\sum_{k=1}^{3} c_k \cos k\phi + s_k \sin k\phi \right].$$

The coefficients c_k and s_k are calculated for large inclinations i and to first order in the ellipticity of the orbits ε_R by Franx, van Gorkom, & de Zeeuw (1994):

$$c_1 = -\varepsilon_R \cos 2\phi_{\rm obs}\,, \quad s_1 = (1 - A - B)\varepsilon_R \sin 2\phi_{\rm obs}\,,$$
$$c_2 = 0\,, \quad s_2 = 0\,,$$
$$c_3 = 0\,, \quad s_3 = (-A - B)\varepsilon_R \sin 2\phi_{\rm obs}\,.$$

The angle $\phi_{\rm obs}$ is measured from the long axis of the orbits (short axis of the potential) to the line of sight. The terms A and B relate to the slope of the rotation curve and the inclination at a given R; if $v_c \sim R^{\alpha}$ and with $q \equiv \cos i$ then

$$A = \frac{1}{2}\frac{\alpha}{1+\alpha}\,, \quad B = \frac{(1-q^2)[3q^2 + 1 - 2A(q^2+1)]}{(1-q^2)^2 + (3q^2+1)^2}\,.$$

Unfortunately, the above equations are only valid when the true parameters (P.A., inclination, circular velocity, and center) are used. These, of course, are returned by the tilted-ring model as only approximate values precisely because it *assumes* $c_1 = 0$ (zeroth-order fit). The second-order harmonics vanish when the true center is used, and the remaining coefficients are calculated assuming this. Franx et al. also show that the tilted-ring model returns the true inclination if the rotation curve is flat, causing the c_3 term to vanish. All information about c_1 is lost in the zeroth-order tilted ring fit, so instead of information about both $\varepsilon_R \cos 2\phi_{\rm obs}$ and $\varepsilon_R \sin 2\phi_{\rm obs}$, which would allow the separate determination of ε_R and $\phi_{\rm obs}$, only information about $\varepsilon_R \sin 2\phi_{\rm obs}$ is available. The calculated coefficients are different if the disk parameters are derived from the photometry rather than the kinematics, and allow the determination of both the ε_R and $\phi_{\rm obs}$. However, the inclination found from the photometry often differs by $>5^{\circ}$ from that found from the kinematics, making the overall determination uncertain.

The residual velocity field was fitted with

$$\delta v = v_c \sin i \left[s_1 \sin \phi + s_3 \sin 3\phi \right]$$

for s_1 and s_3 for each tilted-ring model annulus, providing three separate, but not independent, estimates of $\kappa = \ell \sin 2\phi_{\rm obs}$. These are shown in Figure 12. The first estimate is simply $\kappa = s_1 - s_3$. The remaining two come from solving for κ from s_1 and s_3 separately under the assumption of a flat rotation curve ($A = \alpha = 0$), and using the known inclination to find B. A fit was performed rather than a Fourier analysis because at certain radii there are gaps in the residual velocity field which makes the Fourier analysis impractical.

Although two of the three estimates depend on the rotation curve being flat, they are actually in good agreement over a surprisingly large range of R. At small R, the lack of agreement between the estimates is likely due to the steep slope of the rotation curve which is not well resolved at our pixel size. At large R (and throughout N2417) large gaps appear in the velocity field. Both of these effects result in s_3 being ill-determined. For any galaxy, the value of κ fluctuates greatly with R, though where the three estimates agree, the values are $\lesssim 0.1$, in line with the estimate of ε_R found by Franx et al. The variation may be due to a changing ellipticity or due to the changing disk geometry affecting $\phi_{\rm obs}$. Density wave streaming possibly could account for the change in disk geometry. Local sources of residual velocities do not account for the variation of κ with radius. Correlations between the residual velocities and the intensity and dispersion images are with the small-scale structure and should have little or no influence on low-order harmonics.

The plots in Figure 12 can be used to estimate the size of mean ellipticities of the galaxies. This was done by assuming that ℓ was constant between galaxies and that viewing angles, $\phi_{\rm obs}$, were randomly distributed. The average value of κ for each galaxy was taken over the range where the three estimates agreed, and these appear in Table 4. Since the mean of $\sin 2\phi = 0$, the rms values were used for comparison—$\kappa_{\rm rms} = \ell[\sin 2\phi_{\rm obs}]_{\rm rms} = \ell/\sqrt{2}$. This gives a mean ellipticity of $\varepsilon_R = 0.059 \pm 0.024$, so the ellipticities are most likely $\lesssim 0.08$, which is consistent with that found by Franx & de Zeeuw (1992). This implies that possible streaming motions associated with flattened dark matter halos are small and do not effectively contribute to the observed scatter in the TF relation. These values are significantly smaller than have been inferred based on the anisotropy of the stellar distribution function in some ellipticals and bulges (e.g., Gerhard et al. 1998). Our implied flattenings are also much smaller (by several factors) than the strongly triaxial halos in cosmological N-body simulations (e.g., Dubinski & Carlberg 1991). This may be an indication that disks dominate the dynamics inside the optical radii of galaxies and that the presence of a strong disk serves to circularize the potential. This is consistent with disks being maximal.

4. SUMMARY

Two-dimensional velocity data provide detailed information about the structure of spiral galaxies. In this paper we have used relatively state-of-the art reduction schemes on Fabry-Perot data, taken at Hα to produce precision velocity fields of seven late-type spiral galaxies. These velocity fields have a linear resolution of 0.5–1.0 kpc, which is substantially higher than 21 cm data can provide. This data set allows us to probe many interesting areas of disk galaxy kinematics. In this, the first paper of a series, we have focussed attention on detecting small-scale noncircular motions and assessing the larger scale rms noise that is present in the velocity fields. Part of the motivation for this particular investigation lies in establishing the degree to which disk galaxies are truly circularly symmetric. Interpretation of the TF relation implicitly assumes this is the case. If it is not, systematic errors can arise. Based on examination of these seven galaxies we reach the following conclusions:

1. The tilted-ring model method does a good job of reproducing the observed velocity fields of spiral galaxies and are only modestly influenced by the presence of noncircular motions. Both the kinematic modeling and the presence of small-scale structure in the velocity fields of the galaxies examined point to galaxies being more complicated, on small scales, than simple differentially rotating disks. The observed small-scale structure in the velocity field is real and not an artifact of the reduction procedures,

since the line-of-sight velocity is independent of whether the line profiles of the Fabry-Perot data are modeled as a Voigt or Gaussian function. Averaged over the disk of the galaxy these small-scale effects contribute 10–15 km s^{-1} of random noise, indicating that velocity fields on the large scale are relatively quiescent.

2. A likely source of the small-scale noncircular motions is kinematic feedback to the gas from regions of star formation. However, there is little evidence that suggests the larger scale velocity dispersion of the gas is effected by overall star formation rate. This is good news for the TF relation as it suggests that the star formation rate is not a secondary parameter. While this has been indirectly tested in the past (there is no color dependence on residuals from the TF relation), this study is perhaps the first to address this issue on a strictly kinematical basis using kinematical data.

3. We examined a subset of the velocity fields for evidence of triaxiality and detect only a small degree. This is at odds with what has been observed for the case of some spiral bulges and/or ellipticals and suggests that in our disk dominated systems, the disk indeed provides a large fraction of the mass inside the optical radius. In this case, the disk would then serve to circularize the potential in the azimuthal sense thus minimizing velocity residuals in the plane of rotation. This supports Kent's (1986, 1987) conclusion that a maximum disk is consistent with the rotation curves of spiral disks. It is certainly possible, though, for the disk to somewhat less than maximal and for it still to (nearly) circularize the potential inside the optical radius. If this is the case, the P.A. misalignment between the inner and outer optical disk could be evidence of a transition between luminous and dark matter dominated regions. Interestingly, two galaxies in our sample show evidence for this effect.

4. The noisy correlation between the photometric and kinematic properties of our sample disk galaxies is cause for some concern in the application of the TF relation. While large-scale averages are in agreement, on small scales, there are significant differences in position angle and orientation of the photometric versus kinematic structure. As such differences are not strongly correlated with where the residual velocities appear, it seems that more than just spiral structure is the cause of these differences. This means that the details of the rotation curve can be quite sensitive to the presence of noncircular motions and/or a variable kinematic center with radius (cf. Persic & Salucci 1988, 1990). Indeed, the variable center kinematic model provides a significantly better match to the observed velocity field, especially in terms of the symmetry of the rotation curve. This is explored in detail in Paper II of this series where it is argued that the variable center is mostly likely the reflection of a clumpy mass distribution in the interior regions of disks. As the light distribution is clumpy there as well, this may provide another indication that maximal disks are present in high surface brightness spiral galaxies.

We thank the referee, Brent Tully, for a careful reading of this manuscript. We also thank conversations with Chris Mihos and Ben Weiner regarding fitting line profiles. Support for this project was enabled by the Miller Trust Fund for support of astronomical research at the University of Oregon.

REFERENCES

Adler, D., & Westphal, D. 1996, AJ, 111, 735
Amram, P., Balkowski, C., Boulesteix, J., Cayatte, V., Marcelin, M., & Sullivan III, W. T. 1996, A&A, 310, 737
Amram, P., Le Coarer, E., Marcelin, M., Balkowski, C., Sullivan III, W. T., & Cayette, V. 1992, A&A, 263, 69
Athanassoula, E. 1984, Phys. Rep., 114, 391
Beauvais, C. 1997, Ph.D. thesis, Univ. Oregon
Bonnarel, F., Boulesteix, J., Georgelin, Y., Lecoarer, E., Marcelin, M., Bacon, R., & Monnet, G. 1988, A&A, 189, 59
Bosma, A. 1981, AJ, 86, 1791
Bothun, G., & McGaugh, S. 1999, preprint
Bureau, M., Mould, J. R., & Staveley-Smith, L. 1996, ApJ, 463, 60
Canzian, B., & Allen, R. 1997, ApJ, 479, 723
Caulet, A., et al. 1992, ApJ, 388, 301
Cecil, G., Wilson, A., & Tully, R. B. 1992, ApJ, 300, 365
Corradi, R., Boulesteix, J., Bosma, A., Amram, P., & Capaccioli, M. 1991, A&A, 90, 121
Cornell, M. E., Aaronson, M., Bothun, G., & Mould, J. 1987, ApJS, 64, 507
Courteau, S., & Rix, H. 1999, ApJ, 513, 561
Davoust, E., & de Vaucouleurs, G. 1980, ApJ, 242, 30
Deharveng, J. M., & Pellet, A. 1975, A&A, 38, 15
de Vaucouleurs, G., & Pence, W. 1980, ApJ, 242, 18
Devost, D., Roy, J. R., & Drissen, L. 1997, ApJ, 482, 765
Dubinski, J., & Carlberg, R. G. 1991, ApJ, 378, 496
Dubout, R., Laval, A., Maucherat, A., Monnet, G., Petit, M., & Simien, F. 1976, Astrophys. Lett., 17, 141
Duval, M., Monnet, G. Boulesteix, J., Georgelin, Y., Le Coarer, E., & Marcelin, M. 1991, A&A, 241, 375
Franx, M., & de Zeeuw, T. 1992, ApJ, 392, L47
Franx, M., van Gorkom, J., & de Zeeuw, T. 1994, ApJ, 436, 642
Gerhard, O., Jeske, G., Saglia, R. & Bender, R. 1998, MNRAS, 295, 179
Giovanelli, R., et al. 1997, AJ, 112, 22
Gottesman, S. T. 1982, AJ, 87, 751
Jedrzejewski, R. 1987, MNRAS, 226, 747
Jimenez-Vicente, J., Battaner, E., Rozas, M., Castaneda, H., & Porcel, C. 1999, A&A, 342, 417
Kent, S. 1986, AJ, 91, 1301
———. 1987, AJ, 93, 816
Landolt, A. 1983, AJ, 88, 439
Lyakhovich, V., Fridman, A., Khoruzhii, O., & Pavlov, A. 1997, Astron. Rep., 41, 447
Marcelin, M., Boulesteix, J., Courtes, G., & Milliard, B. 1982, Nature, 297, 38
Marcelin, M., Boulesteix, J., & Georgelin, Y. P. 1985, A&A, 151, 144
Marcelin, M., Lecoarer, E., Boulesteix, J., Georgelin, Y., & Monnet, G. 1987, A&A, 178, 91
Martin, C. 1997, ApJ, 491, 561
Martin, C., & Kern, B. 1999, ApJ, submitted
McGaugh, S., & de Blok, E. 1998, ApJ, 499, 41
Mihos, J. C., & Bothun, G. 1997, ApJ, 481, 781
———. 1998, ApJ, 500, 619
Pence, W., Taylor, K., & Atherton, P. 1990, ApJ, 357, 415
Pence, W., Taylor, K., Freeman, K., de Vaucouleurs, G., & Atherton, P. 1988, ApJ, 326, 546
Persic, M., & Salucci, P. 1988, MNRAS, 234, 131
———. 1990, ApJ, 356, 83
Regan, M., Teuben, P., Vogel, S., & van der Hulst, T. 1996, AJ, 112, 2549
Rots, A. 1975, A&A, 45, 43
Ryder, S., Zasov, A., Sil'chenko, O., Mcintrye, V., & Walsh, W. 1998, MNRAS, 293, 411
Sackett, P. 1997, ApJ, 483, 103
Sackett, P., Rix, H., Jarvis, B., & Freeman, K. 1994, ApJ, 436, 629
Sakai, S. et al. 1999, ApJ, in press
Schommer, R., Bothun, G., Williams, T. B., & Mould, J. 1993, AJ, 105, 97 (SBWM)
Schommer, R., Caldwell, N., Wilson, A., Baldwin, J., Phillips, M., Williams, T., & Turtle, A. 1988, ApJ, 324, 154
Sicotte, V., Caignan, C., & Durand, D. 1996, AJ, 112, 1423
Teuben, P., Sanders, R. H., Atherton, P., & van albada, G. 1986, MNRAS, 221, 1
Thornley, M., & Mundy, L. 1997, ApJ, 490, 682
Tully, B. 1972, Ph.D. thesis, Univ. Maryland
———. 1974, ApJS, 27, 415
Tully, B., & Fouqué, P. 1985, ApJS, 58, 67
Turner, J., & Hurt, R. 1992, ApJ, 384, 72
Unger, S., Taylor, K., Pedlar, A., Ghataure, H., Penston, M., & Robinson, A. 1990, MNRAS, 242, 33
van der Hulst, J. M. 1979, A&A, 75, 97
Veilleux, S., Cecil, G., & Bland-Hawthorn, J. 1995, ApJ, 445, 152
Vogel, S., Rand, R., Gruendl, R., & Teuben, P. 1993, PASP, 105, 666
Williams, T., Caldwell, N., & Schommer, R. 1984, ApJ, 281, 579
Yuan, C., & Chen, Y. 1989, ApJ, 340, 216